Ludwig-Maximilians-Universität, München
Chair for Theoretical Condensed Matter Physics of Prof. Jan von Delft and Prof. Stefan Kehrein
Theresienstr. 37
80333 München
Germany

Graphene
ultra-relativistic massless particles in carbon layers

Bachelor Thesis
Supervisor: Prof. Jan von Delft

Korbinian Paul
19. April 2008

April 22, 2008

Contents

Abstract

This text is an introductory review about graphene, a two dimensional layer of graphite crystals. The stability of two dimensional crystals is addressed by the Mermin-Wagner theorem which excludes long range order for two dimensional systems. However, experiments, simulations and the theory of polymerized membranes hold the formation of ripples responsible for the stability. From the tight binding model the dispersion relation is derived, describing massless, ultra-relativistic particles in the low energy limit. Furthermore, the low energy expansion is driven to a real QED like description, which is compared to massless neutrinos. Finally, the integer quantum Hall effect, appearing at a half-integer sequence and at room temperature shows that the underlying relativistic structure of the quasi particles is responsible for the unconventional Hall quantization. Hence, knowledge and methods from high-energy physics like the Atiyah-Singer index theorem are applicable, showing that graphene is really a condensed matter realisation of ultra-relativistic particles.

Acknowledgements

1 Introduction

Graphene, one layer of graphite is a hot topic in solid state physics which extends the diversity of two dimensional electron systems. Long time before A. Geim and K. Novoselov obtained the first graphene flakes at Manchester University with micro mechanical cleavage it was an object of research. Nevertheless, since its discovery, graphene invaded the solid state and material science community and let to some unexpected physics. In conceptual respect, graphene is the starting point of other carbon allotrops like nanotubes and fullerens. Furthermore, graphene connects high energy particle physics with low energy condensed matter physics, allowing table top observation of relativistic particles. Electrons at low energies behave like ultra relativistic massless particles moving with an effective speed of light $v_F \approx 10^6 m/s$. Moreover it exhibits a quantum phenomenon which is still present at room temperatures, namely the quantum Hall effect. Besides these features graphene may be a possible candidate for a ballistic field effect transistor which would give perspectives for electronics beyond silicon. Finally, carbon shows once more that it is possibly the most fascinating element of nature dominating large parts of science.

1.1 How to get graphene?

Graphene and other two dimensional materials like BN, MoS_2, $NBSe_2$ and $Bi_2Sr_2CaCu_2O_x$ are produced by micromechanical cleavage [21], a process of such a conceptual simplicity, that it almost seems absurd that two dimensional crystals still were undiscovered until recently. Naivily spoken, micromechanical cleavage is compareable to "drawing by chalk on a blackboard" and then seeking for monolayer flakes. Most of the efforts to gain two dimensional structures, that were done before Andre Geim and Kostya Novoselov from Manchester University in the UK discovered graphene in 2004, used chemical exfoliation of strongly layered materials. For instance graphite, where the in plane bonds are very strong compared to the weak van der Waal-like coupling between those layers. This type of a three dimensional crystal, arranged in layers, is necessary as a raw material for the micromechanical claevage process.

The two dimensional (2D) crystallites (graphene) are extracted by rubbing of a 3D layered crystal (graphite) onto another surface. There are no bizarre requirements on that surface, it could be any solid surface. The rubbing process produces thin flakes and we just have to look for monolayers. But the identification of single layered structures is exactly the crucial step, that was responsible for the rather late discovery of graphene [21]. One should mention that monolayer crystals are a small minority of the flakes gained by cleavage. Secondly, besides the edges of the flakes, there is no significant structure visible in transmission electron microscope (TEM) images fig.(3) and hence no difference between single

and few layer crystals. Furthermore, on most of the common substrates used like glass or metal, it is not possible to observe monolayer structures. The atomic force microscope (AFM) is the only tool to detect monolayer films on a substrate directly, but in practice, it would be impossible to search for graphene by scanning the whole surface.

The trick is to put the flakes on an oxidized Si waver, where they become visible in an conventional optical microscope. Figure(1) shows several graphitic flakes on SiO_2 viewed by optical microscopy. The SiO_2 surface reflects the whole "rainbow-spectrum" of coulors. In addition, even a monolayer adds up sufficiently to the optical path of reflected light. Hence, similar to oil films, the interference colour changes if light is reflected by a flake compered to the colour of light reflected by the substrate. In this way single layers have an observable contrast on the surface. Moreover, there are high requirements on the SiO_2 wavers. If for example the thickness varies within 5% [1] then single layer graphene is completely invisible [4].

After a graphene flake has been found one can start further observations with TEM or AFM.
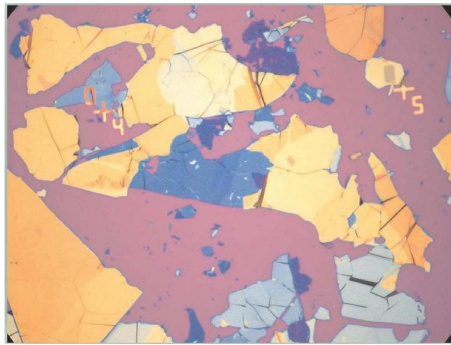
Figure 1: graphite flakes of different thickness rubbed from graphit onto a SiO_2 surface where it is visible for an optical microscope(Physics Today, August 2007, A. Geim, A.H. MacDonald

To sum up the fabrication of graphene so far, we have seen that two dimensional crystals are gained by micromechanical cleavage and found on a SiO_2 substrate with optical microscopy. This is actually the starting point of every experiment. Moreover, the two dimensional crystals produced in that way are stable under ambient conditions and exhibit high crystal quality [21], so they can be used to study the quantum Hall effect (QHE) and transport properties. Since march 2007, graphene samples can be bought from a company called graphene industries[2] at rather high prices compared with their size. A big flake of $5500 \mu m^2$ ($\pm 10\%$ de-

---

[1]for the standard $300nm$ thickness this is equivalent to a deviation within $15nm$

[2]http://www.grapheneindustries.com

viation) costs 2500£! Although micromechanical cleavage is a successful method to obtain graphene, there should be a more effective way of manufacturing large amounts of graphitic sheets, if one day micro electronics will be made of carbon.

2 Stability of graphene

The honeycomb structure of single graphite layer comes from the strong covalent binding. Carbon is in the fourth column of the periodic table of the elements and has six electrons in the groundstate configuration $1s^2 2s^2 2p^2$. Plugged in the lattice, the $2s, 2p$ electrons form an sp^2 hybrid orbital, where three electrons are localised. As one can see in figure(2), these electron clouds are in a plane, including angles of $120°$. By overlapping those sp^2 orbitals of neighbouring atoms one gets the strong binding σ-orbitals. These orbitals do not contribute to the conductivity. The last electron becomes the free charge carrier by forming a π-orbital which is delocalized and perpendicular to the lattice plane.

Furthermore, graphene can be described by a two dimensional Bravais lattice
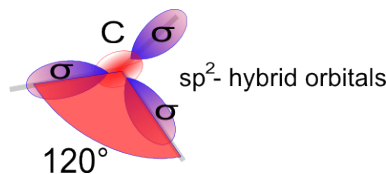
Figure 2: sp^2 - hybrid orbitals of carbon, origin of the honeycomb structure. Their overlapp with orbitals of other carbon atoms form the strong σ bonds, including an angle of $120°$

with a two atomic basis, but we will pick up that discussion later on, when we derivate the electronic dispersion relation.

2.1 Instability of Two dimensional Crystals in General

As we have already noted, it can be shown that two dimensional crystals are in general unstable. This was done in different ways by Landau, Peierls and Mermin, just to mention a few, and in the following Mermin's argument [15] will be briefly scatched.
The background of all these arguments is the absence of phase transitions in certain low dimensional systems. For instance, Mermin and Wagner [16] showed that there is no spontaneous magnetisation in an isotropic Heisenberg model with finite range interaction. Moreover, for classical systems in one dimension it can be proven that there are no phase transitions, if only finite range interactions are

considered. Nevertheless, Thouless and Kosterlitz [13] showed that phase transitions in two-dimensional systems where no long-range order of the conventional type exists are still possible. In that sense, we have to give up long range translational order and define an other so called topological order.

This formal discussion is of some importance because we will use Bloch's Theorem later on to calculate the electronic band-structure. That means we assume long-range translational order. As we will see, this is not obvious. In any case these arguments appeared on most of the recent publications about graphene, hence one should have a closer look to them.

The aim of Mermin's argument is to show that there is no long-range order in true two dimensional systems. Physically spoken, with increasing number of particles N, certain criteria or properties defining a crystals are no longer fulfiled. In addition, the argument includes only crystals with short-range pair potentials $\Phi(\vec{r}_1 - \vec{r}_2)$ like the Lennard-Jones potential[3], but it excludes for example the hard-sphere potential and the Coulomb potential. So, the first task is to choose an appropriate criterion for the presence of order.

Our Bravais lattice is spanned by the lattice vectors $\vec{a}_1$ and $\vec{a}_2$ for example the lattice vectors of the honeycomblattice. Then a point of the Bravais lattice is discribed by $\vec{r} = N_1\vec{a}_1 + N_2\vec{a}_2$, where $N = nN_1N_2$ is the number of particles, n is the number of particles of the basis.

For the density of our crystal particles we write

$$\hat{\rho}(\vec{r}) = \sum_{i=1}^{N} \delta(\vec{r} - \vec{r}_i) \tag{1}$$

$$\hat{\rho}_{\vec{k}} = \int d\vec{r} e^{-i\vec{k}\cdot\vec{r}} \hat{\rho}(\vec{r}) = \sum_{i=1}^{N} e^{-i\vec{k}\cdot\vec{r}_i} \tag{2}$$

In equation(2) we have introduced the k-th Fourier component of the density. Furthermore, we need the thermodynamical average of equation(2).

$$\rho_{\vec{k}} = N^{-1}\langle\hat{\rho}_{\vec{k}}\rangle \tag{3}$$

Following from these definitions, we are able to construct our criterion for crystallinity:

- $\lim_{N\to\infty} \rho_{\vec{k}} = 0$, if $\vec{k}$ is not a reciprocal-lattice vector

- $\lim_{N\to\infty} \rho_{\vec{k}} \neq 0$, for at least one nonzero reciprocal lattice vector

One may varify this by using the definition of reciprocal lattice vectors[4] $\vec{K}$. This is exactly the statement of long-range translational order.

---

[3]Lennard-Jones potential: $\sim \frac{\sigma}{r^{12}} - \frac{\tau}{r^6}$

[4]$\vec{r}$ is a lattice vector if $\vec{K} \cdot \vec{r} = 2\pi$

The next step is to estimate $\rho_{\vec{K}}$ ($\vec{K}$ reciprocal lattice vector) from above with the help of an inequality following from the well-known Schwartz inequality:

$$\langle |A|^2 \rangle \geq |\langle A \cdot B \rangle / \langle |B|^2 \rangle$$

The inequality of Mermin's theorem is:

$$\langle |\sum \psi_i|^2 \rangle \geq \frac{k_B T |\sum \langle \varphi_i \nabla \psi_i \rangle|^2}{\langle \frac{1}{2} \sum \nabla^2 \phi(\vec{r}_i - \vec{r}_j) |\varphi_i - \varphi_j|^2 + k_B T \sum |\nabla \varphi_i|^2 \rangle} \tag{4}$$

Now we have to assign functions to ψ_i and φ_i, so that the potential Φ and the Fourier component of the density $\rho_{\vec{k}}$ comes in. Furthermore we introduce the free energy in the inequality. For further estimations, we need the free energy per particles for the pair potential ϕ to be intensive. This is equivalent to the condition that the potential has to be integrabel at infinity, repulsive and nonintegrable at the origin, like the Lennard Jones Potential.

$$\Phi(\vec{r}) \to 1/r^{2+|\epsilon|} \qquad as \qquad r \to \infty$$
$$\Phi(\vec{r}) \to const./r^{2+|\epsilon|} \qquad as \qquad r \to 0$$
$$\tag{5}$$

In the end we get an estimate for $\rho_{\vec{K}}$, where $\vec{K}$ is a vector of the reciprocal lattice.

$$\rho_{\vec{K}} \leq \frac{const.}{(\ln N)^{1/2}} \tag{6}$$

$\rho_{\vec{K}} \to 0$ as $N \to \infty$. That means in the thermodynamic limit, there is no positional long-range order. However directional long-range order is still present. The constant in eq.(6) is proportional to a characteristic energy ϵ devided by the Temperature:

$$const. \propto \frac{\epsilon}{k_B T} \tag{7}$$

Now the length of the biggest graphene samples[5] is about $L = 100\mu m$. Typical experiments are done at very low temperatures. So let us assume that $T = 1K$ in equation(7). With $L = N \cdot a_0$, equation (6) and (7) one can estimate a lower bound for the characteristic energy ϵ. The result is $\epsilon > 1meV$, a value much lower than typical bond energies. This would guarantee the stability, long-range order, of graphene for a finite size of the samples.
It can be shown [20] that the condition $\langle |u|^2 \rangle < a_0 < \infty$ for the displacement implies our condition for cristallinity above, but not vice versa.
Now in which way does this theorem address graphene?

---

[5] One can by graphene samples at *www.grapheneindustries.com*. For example a sample of about $75\mu m \times 75\mu m$ is sold for 2500 pounds.

On the one hand interactions are less short ranged than in metals because screening effects are not so strong due to the smaller charge carrier concentration. Moreover graphene could be metastable [4], but with such a long lifetime that it is irrelevant to observe this in an experiment.

On the otherhand, in order to exist, graphene is randomly rippled. We will see in the next section why corrugations of graphene sheets are related to stability of graphene.

2.2 Why does Graphene exist?

First attempts to answer the question why graphene exists are surprisingly not given by solid state theory, but there is a qualitative answer from Soft-Condensed Matter Theory. With a continuous model of polymerized membranes embedded in three dimensions P. Le Doussal and Leo Radzihovsky [14] showed by using a self-consistent screening approximation that flat membranes exist. As a result, these membranes are not perfectly flat, but they have intrinsic ripples. Indeed, corrugations of graphene flakes have been observed [17] and they are influencing some electronic properties like weak localisation[6] [18]. However, the results of these theories cannot quantitatively describe the ripples, and only agree with the simulations [3] within a certain frame. Corrugations are a typical feature of monolayer graphene while they become smaller in bilayer and vanish in multilayer graphene.

At first we will have a short look at an experiment [17] which examined freely suspended graphene flakes for the first time. Graphene becomes visible on a SiO_2 surface with an optical microscope and in most of the other experiments done so far, graphene has always been a part of a three dimensional structure.

The observations done here prove, that freely suspended graphene can exist without a substrate and has random elastic deformations into the third dimension.

After a monolayer of graphene was identified on the SiO_2 substrate, a metal grid was deposited on top of the flake by using electron beam lithography. Secondly, the SiO_2 support was etched away. Figure(3) shows a bright-field transmission electron microscope (TEM) image of the suspended graphene flake attached to the metal grid. The scale bar shows that there is a more than $500nm$ spacing between the grid, which is magnitudes larger then the lattice constant. Hence we are really observing freely suspended graphene.

Furthermore TEM electron diffraction experiments have been done. At first this may seem useless because a two dimensional crystal only acts as a plane

---

[6]weak localisation (wl) is responsible for quantum interference correction to the conductivity due to interference between time reversed paths

Figure 3: A freely suspended graphene flake attached to a micrometer-sized metallic scaffold. The regions indicated by the arrows are monolayer graphene. On the righthand side there is a folded part of the sheet visible. The scale bar is $500nm$ large.

reflecting the electron beam at the position of the atoms[7]. Therefore only the direct reflection, the zeroth order diffraction peak is visible independent from the incident angle. Nevertheless electron diffraction experiments are very useful to distinguish monolayer from bilayergraphene. Due to the second layer in bilayergraphene, one observes a diffraction pattern with maxima and minima at certain tilt angles in contrast to the monolayer case. This is visualised in figure(4).

This experiment would be less spectacular, if the diffraction pattern of the singlelayer graphene wouldn't contain some unexpected features.

The first two pictures 1 of figure(4) show a broadening of the diffraction peaks of singlelayer graphene with increasing tilt angle. This behaviour vanishes for an increasing number of layers. It is well-known in X-ray diffraction that only the intensity of the diffraction peaks will be affected by thermal vibrations, not their extent. The reason for the blurred diffraction spots are random corrugations on the submicrometer level in graphene.

Diffraction patterns are given by a two-dimensional slice through the three dimensional Fourier transform of the crystal. For a perfectly flat crystal this Fourier transform is a set of rods perpendicular to the reciprocal lattice. These rods wander around their average direction, forming cones when the sheet is slightly corrugated. Regarding figure(5) the cross-section of the diffraction peaks under different incident angles is given by the intersection of the cones with the tilted plane. The tilted planes are related to the incident angles.

Comparisons with simulations of the diffraction patterns give some quantitative

---

[7]Actually the graphene sheet acts like a grid, but without another layer, there is no incident angle dependend interference. Hence, an interference pattern is still visible, but it has no information about incident angles.
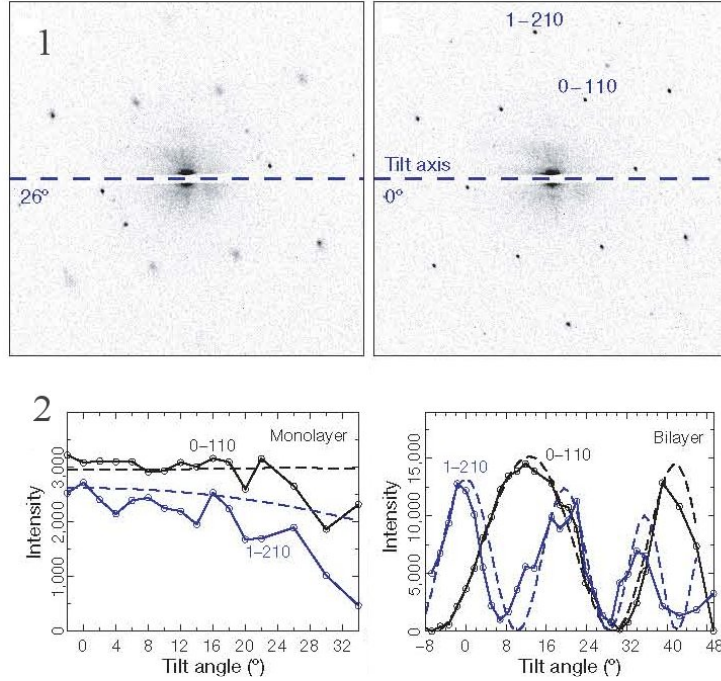
Figure 4: (1) TEM diffraction pattern of monolayer graphene for two different incidence angles, 26° (right) 0° (left). The diffraction peaks of the right image are broadend compered with those from the left. (2) Total intensity as a function of tilt angle of the two peaks $(0-110)$ and $(1-210)$ of monolayer (right) and bilayer (left) graphene.

estimates about the ripples in graphene. The ripples are about $1nm$ high and have a spatial extent of $2-20nm$. In atomic-resolution TEM imaging ripples have been observed directly in two and more layer graphene[8]. These observations support the estimates above. Moreover the fact, that corrugations can be observed directly with TEM means that it is a static phenomenon.

Of course, the term freely suspended means spanned on a scaffold. And all the other experiments done so far used supproted graphene. The support gives boundary condition and may induce stability and translational order. But then the ripples have to carry some signatures from the boundaries. To my knowledge, no experiment so far has refered to the observation that ripples have a significant dependence on the boundaries.

We have already heard that the theory of polymerized membranes gives a partly explanation of the formation of ripples in flexible membranes [14]. Membranes of internal dimensionality D with linear size L, embedded in a d dimensional space, are characterized by a roughness exponent ζ. In this way transverse dis-

---

[8]For monolayer graphene there is not enough contrast to make ripples directly visible. Because diffraction intensities vary only little with tilt angle
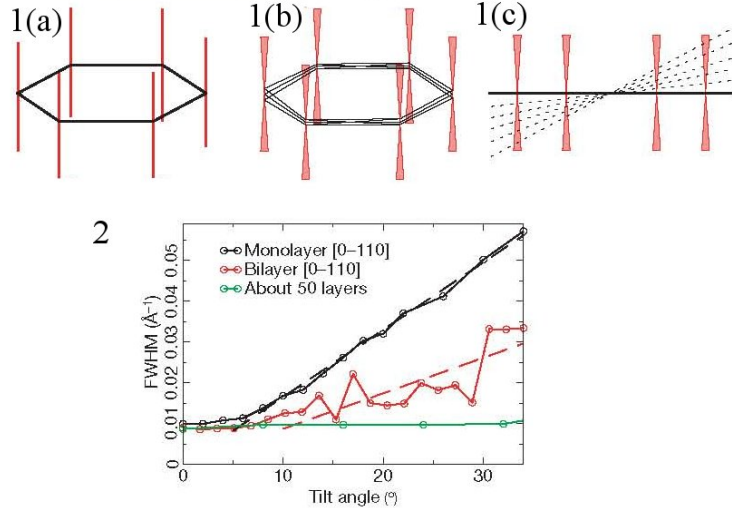
Figure 5: (1) origin of the peak broadening with increasing tilt angles in the diffraction images. The continuous rods represent the intensities in reciprocal space. Intersections with the tilted plain (dotted line) give a peak in the diffraction pattern. In the case of a corrugated surface the rods become cones. (2) FWHM of diffraction peaks versus tilt angles

placements scale as L^ζ, and for flat physical membranes ($D = 2$, $d = 3$) they predict a roughness exponent of $\zeta = 0.590$. Furthermore critical parameters for a transition from the flat to the crumbled phase were analysed.

We will have a brief look at this theory:

A D dimensional membrane with internal coordinates $\vec{x}$ exhibits both a D component in-plane phonon field $u_\alpha(\vec{x})$, $\alpha = 1 \dots D$, and out-of-plane displacements $\vec{h}(\vec{x})$ [9].

The free energy is a sum of bending and in-plane elastic energy.

$$F = \int d^D x \left[\frac{\kappa}{2} (\nabla^2 \vec{h})^2 + \mu U_{\alpha\beta}^2 + \frac{\lambda}{2} U_{\alpha\alpha}^2 \right] \tag{8}$$

The coefficient κ is the bending rigidity, μ is the shear modulus and λ is the first *Lamé* parameter which is also related to linear elasticity. $U_{\alpha\beta}$ is the strain tensor

$$U_{\alpha\beta} = \frac{1}{2} \left(\frac{\partial u_\beta}{\partial x_\alpha} + \frac{\partial u_\alpha}{\partial u_\beta} + \frac{\partial \vec{h}}{\partial x_\alpha} \cdot \frac{\partial \vec{h}}{\partial x_\beta} \right) \tag{9}$$

Here it is important to note that the in-plane stresses and out-of-plane displacements are non-linear coupled, because the strain tensor (9) contributes quadratically to the free energy (8). By neglecting the last term in the strain tensor

---

[9]for physical membranes $\vec{h} = h$ and u_α, $\alpha = 1, 2$ has two components

(9) the bending h and stretching modes u_α become decoupled and one is in the harmonic approximation regime.

In the harmonic approximation, where the last term in eq.(9) is neglected, the mean square angle between the normals of the membrane $\langle |\vec{n}|^2 \rangle$ diverges with the sample size $L \to \infty$ and for long wavelength phonons, which indicates a tendency to crumple.

If the anharmonic coupling term is taken into account, the flat phase remains stable but is corrugated. The curvature fluctuations soften elastic constants and screen the phonon mediated interaction. As a result the long wavelength fluctuations are suppressed, which eliminates the divergency from above. The roughness of the membranes is given by L^ζ where $\zeta \approx 0.6$. However, one should deal with that result carefully. Because it still predicts that these height fluctuations grow with the sample size and can be anomalously large. Moreover there are other predictions from Soft-Condensed Matter Theory like spontaneous creation of dislocations [3] which are neither observed in experiments [17] nor in simulations [3].

Recently there has been an attempt to explain the origin of ripples [3] by A. Fasolino, J.H. Los and M.I. Katsnelson. They did atomistic Monte Carlo simulations using an effective many body potential LCBOPII (Long-range Carbon Bond Order Potential 2) which is said to provide a unified description of the energetics and elastic constants of all carbon phases with an accuracy compareable to the experiment. Because of being a long-range potential, we can not apply Mermin's Theorem in that case- It requires short-range potentials. Moreover, they used the normal-normal correlation function and the temperature dependence of the bending rigidity κ as observables to oncompare the simulations with the Theory of polymerized membranes. They conclude that the ability of carbon to form different types of bonding (fig.(6)) is responsible for the difference between graphen sheets and a generic two-dimensional crystal. In addition, one has to take atomic properties in onto account because there are properties in graphene which are not common to a continuum model of flexible membranes.

So far, the problem of the stability of graphene and the origin of its corrugations has not been solved completely.

3 Electronic properties of Graphene

3.1 The Dispersionrelation of Graphene

The dispersion relation $\epsilon(\vec{k})$ is a very important quantity in Solid State Theory. We can not only extract a lot of information about the charge carriers from it, but all semi-classical calculations are also based on its knowledge. Moreover, one of the most important properties of graphene is the massless dirac fermion-like
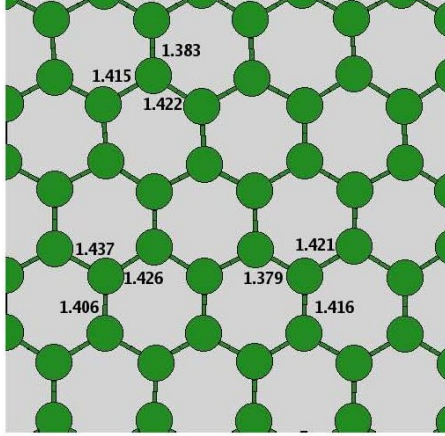
Figure 6: Variation of bond length as an explanation of the ripple formation in graphene.

spectrum, i.e. the linear energy-momentum dependence with zero energy states. This is also a result of the dispersion relation.

We use the compact and elegant formalism of second quantization and the tight-binding approximation to derivate $\epsilon(\vec{k})$. The tight-binding approximation (TBA) is a model for charge carriers, i.e. electrons, in a periodic lattice. The following will be a short introduction to the TBA. Electrons are tightly binded to the Ions at each lattice site, that means their wave functions $|\psi_n\rangle$ must be somewhat similar to wavefunctions in the vicinity of the ions. Moreover the periodic lattice contribution tells us, that an electron state has to fulfil Bloch's Theorem:

$$\Psi_{\vec{k},n}(\vec{r}) = e^{i\vec{k}\cdot\vec{r}}u_{\vec{k},n}(\vec{r}); \qquad u_{\vec{k},n}(\vec{r}+a_0\vec{e}_i) = u_{\vec{k},n}(\vec{r})$$

$$\Psi_{\vec{k},n}(\vec{r}+\vec{R}) = e^{i\vec{k}\cdot\vec{R}}\Psi_{\vec{k},n}(\vec{r}) \tag{10}$$

The full Hamiltonian of that problem is the sum of the atomic Hamiltonian $\mathcal{H}_{at}$ with eigenvalue E_n plus a correction $\Delta U(\vec{r})$ which takes into account all the contributions coming from the periodicity of the lattice.

$$\mathcal{H} = \mathcal{H}_{at} + \Delta U(\vec{r}) \tag{11}$$

$\{\psi_m\}$ is the set of atomic wavefunctions with eigenvalues E_m. They become small in the middle between two lattice sites where $\Delta U(\vec{r})$ becomes appreciable.

$$||\Delta U(\vec{r})\psi_m|| \ll 1 \tag{12}$$

Although, it would be tempting to expand the eigenstates $\Psi_{\vec{k},n}(\vec{r})$ of (11) directly into atomic wavefunctions $\{\psi_m\}$, it would give eigenvalues $\epsilon_n(\vec{k}) \sim E_m$ proportional to the atomic eigenenergies which are obviously not depending on $\vec{k}$. To

16

avoid this deficiency we expand $\Psi_{\vec{k},n}$, our eigenstates of the crystal Hamiltonian (11), in yet unknown functions $\phi(\vec{r})$. These functions ϕ can be expanded in a small number of atomic wavefunctions ψ_m.

$$\Psi_{\vec{k},n}(\vec{r}) = \sum_{\vec{R}} e^{i\vec{k}\cdot\vec{R}} \phi(\vec{r} - \vec{R}) = \sum_{\vec{R}} e^{i\vec{k}\cdot\vec{R}} \sum_{n} b_n \psi_m(\vec{r}) \tag{13}$$

With $\mathcal{H}\Psi_{\vec{k},n} = \epsilon_n(\vec{k})\Psi_{\vec{k},n}$ we get after some calculations the following eigenvalue:

$$\epsilon_n(\vec{k}) = \epsilon_n^0 - \sum_{n.n.} t(\vec{R}) \tag{14}$$

The sum on the righthand side goes over all nearest neighbours (n.n.) of an ion and over all N ions. $t(\vec{R})$ is the overlapp integral and it depends on the distance between two lattice sites. Thus, only the nearest neighbour contributions are relevant because $t(\vec{R})$ becomes small if the ions are increasingly far from each other away. In the limit we have just isolated ions, $t(\vec{R})$ vanishes and we are left with the atomic eigenenergies. This is a fact, we would have expected for self-consitency.

For the sake of simplicity we are only interested in one single band, so we will drop the bandindex in our formulas.

The eigenenergy $\epsilon(\vec{k})$ defined above in eq.(14) gives rise to a model Hamiltonian,

$$\mathcal{H} = \underbrace{\sum_{\vec{r},\sigma} \epsilon_0 \hat{a}_\sigma^\dagger(\vec{r})\hat{a}_\sigma(\vec{r})}_{\mathcal{H}_0} - t \underbrace{\sum_{<\vec{r},\vec{r}'>n.n.} \left(\hat{a}_\sigma^\dagger(\vec{r})\hat{a}_\sigma(\vec{r}') + h.c.\right)}_{\mathcal{H}_{Hop}} \tag{15}$$

where h.c. in the second part of the righthand side means hermitian conjugate, σ accounts for the spin. This part is the so-called hopping Hamiltonian. It describes the contribution coming from the exchange of an electron from lattice site at $\vec{r}$ to lattice site at $\vec{r}'$. Due to the dependence on t it is clear that we restrict ourselves only to nearest neighbours (n.n.).

So far we have just briefly reviewed the tight-binding approximation. To become more concrete, we apply this methode to an infinite or sufficiently large graphene layer[10].

Figure(7) shows the honeycomb of graphene with the lattice vectors and the two atomic basis. Once more the lattice vectors are:

$$\vec{a}_1 = \frac{a_0}{2} \begin{pmatrix} \sqrt{3} \\ 1 \end{pmatrix}; \qquad \vec{a}_2 = \frac{a_0}{2} \begin{pmatrix} \sqrt{3} \\ -1 \end{pmatrix} \tag{16}$$

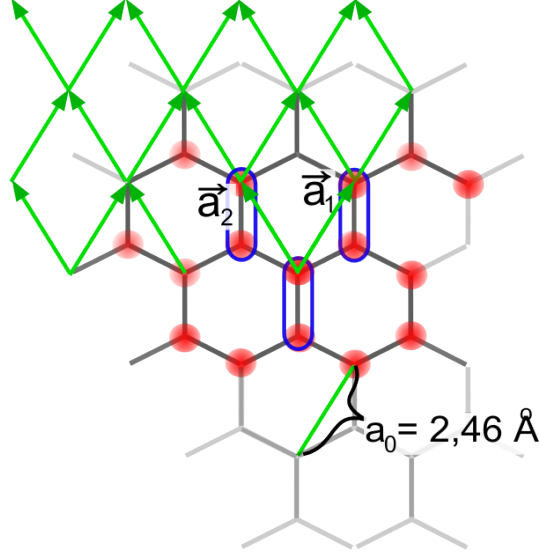[10]we are not interested in effects comming from the edges

Figure 7: Honeycomb structure of graphene (lower right), and the corresponding Bravais lattice (upper left). In the middle, the lattice vectors $\vec{a}_1$, $\vec{a}_2$ are shown together with the two atomic basis. Bond length of carbon atoms 1.42 Angström

The vectors $\vec{G}_i$ of the reciprocal lattice are defined by: $\vec{G}_i \cdot \vec{a}_j = 2\pi\delta_{i,j}$.

$$\vec{G}_1 = \frac{2\pi}{a_0\sqrt{3}} \begin{pmatrix} 1 \\ \sqrt{3} \end{pmatrix}; \qquad \vec{G}_2 = \frac{2\pi}{a_0\sqrt{3}} \begin{pmatrix} 1 \\ -\sqrt{3} \end{pmatrix} \tag{17}$$

The hole system's spatial extent is in $\vec{a}_1$ direction $L_1 = N_1 a_0$ and in $\vec{a}_2$ direction $L_2 = N_2 a_0$. Furthermore we assume periodic boundary conditions. Plane waves $e^{i\vec{k}\cdot\vec{r}}$ have to fulfil $k_i \cdot L_i = 2\pi n_i$, hence the wavevectors are in the intervall $\left[0, \ldots, \frac{2\pi}{a_0}\right]$, i.e. $\vec{k} = \frac{2\pi}{N_2 a_0}n$, $n \in \mathbf{N}$.

The hopping Hamiltonian $\mathcal{H}_{Hop}$ of equation(15) looks slightly different, because of the two atomic basis of graphene crystals. That means we have to distinguish between operators acting on the first atom of a site at $\vec{r}$ or on the second one. We denote this by another index. Which one is the first and which one is the second atom is shown in figure(7). Below, we consider only the hopping part because $\mathcal{H}_0$ is just an energy shift.

$$\mathcal{H}_{Hop} = \sum_{<\vec{r},\vec{r}'>n.n.} t \left(\hat{a}_\sigma^\dagger(\vec{r})\hat{b}_\sigma(\vec{r}') + \hat{b}_\sigma^\dagger(\vec{r}')\hat{a}_\sigma(\vec{r}) \right) \tag{18}$$

$\hat{a}_\sigma^\dagger(\vec{r})$ creates a state in the site of the sublattice A at vector $\vec{r}$

$\hat{b}_\sigma^\dagger(\vec{r}')$ creates a state in the site of the sublattice B at vector $\vec{r}'$

These operators have the following Fourier representation, N is the total number

of lattice sites.

$$\hat{a}_\sigma^\dagger(\vec{r}) = \frac{1}{\sqrt{N}} \sum_{\vec{k}}^{1.B.Z.} e^{-\vec{k}\cdot\vec{r}} \hat{a}_{\vec{k},\sigma}^\dagger \tag{19}$$

$$\hat{b}_\sigma^\dagger(\vec{r}) = \frac{1}{\sqrt{N}} \sum_{\vec{k}}^{1.B.Z.} e^{-i\vec{k}\cdot\vec{r}} \hat{b}_{\vec{k},\sigma}^\dagger \tag{20}$$

The sum is restricted to the first Brillouin zone, hence the components of $\vec{k}$ are in the set $k_i \in \{0, \ldots, \frac{2\pi}{a_0}\}$. Moreover, the vectors $\vec{G}_i$ span the reciprocal lattice. At this point, it is convenient, as a specification of our lattice, to express the wavevectors $\vec{k} = b_1\vec{G}_1 + b_2\vec{G}_2$ in terms of the reciprocal-lattice vectors. Then, the coefficients $b_i = n/N_i$ run from $0 \ldots$ to $\ldots 1$.

$$\vec{k} = b_1\vec{G}_1 + b_2\vec{G}_2 = \frac{a_0}{2\pi}\left(k_1\vec{G}_1 + k_2\vec{G}_2\right) \tag{21}$$

In (21) we have gained a representation of the wavevector $\vec{k}$, where $\vec{k}$ depends on its coefficients $\vec{k}_i = \frac{2\pi}{N_i a_0}n$ and on the reciprocal lattice vectors.
Thus the two types of annihilation and creation operators respectively can be written as

$$\hat{a}_\sigma^\dagger(\vec{r}) = \frac{1}{\sqrt{N}} \sum_{k_1,k_2} e^{-i\frac{a_0}{2\pi}\left(k_1\vec{G}_1 + k_2\vec{G}_2\right)\cdot\vec{r}} \hat{a}_{\vec{k},\sigma}^\dagger$$

$$\hat{b}_\sigma^\dagger(\vec{r}) = \frac{1}{\sqrt{N}} \sum_{k_1,k_2} e^{-i\frac{a_0}{2\pi}\left(k_1\vec{G}_1 + k_2\vec{G}_2\right)\cdot\vec{r}} \hat{b}_{\vec{k},\sigma}^\dagger$$

$$\tag{22}$$

Finally, we plug the operators(19) and (20) into the hopping Hamiltonian equation(18). The Spin index has no influence on the result and will be omitted.

$$\mathcal{H} = \sum_{<\vec{r},\vec{r}'>n.n.} t\left(\hat{a}^\dagger(\vec{r})\hat{b}(\vec{r}') + b^\dagger(\vec{r}')\hat{a}(\vec{r})\right)$$

$$= t\frac{1}{N} \sum_{<\vec{r},\vec{r}'>n.n.} \sum_{\vec{k}} \left(e^{-i\vec{k}(\vec{r}'-\vec{r})}\hat{a}_{\vec{k}}^\dagger\hat{b}_{\vec{k}} + e^{-i\vec{k}(\vec{r}-\vec{r}')}\hat{b}_{\vec{k}}^\dagger\hat{a}_{\vec{k}}\right)$$

$$= t\sum_{\vec{k}} \left(\left(e^{i\vec{k}\vec{\delta}_1} + e^{i\vec{k}\vec{\delta}_2} + e^{i\vec{k}\vec{\delta}_3}\right)\hat{a}_{\vec{k}}^\dagger\hat{b}_{\vec{k}} + \left(e^{-i\vec{k}\vec{\delta}_1} + e^{-i\vec{k}\vec{\delta}_2} + e^{-i\vec{k}\vec{\delta}_3}\right)\hat{b}_{\vec{k}}^\dagger\hat{a}_{\vec{k}}\right) \tag{23}$$

In the last step we carried out the nearest neighbour (n.n.) summation in the way shown in figure(8). The k-sum runs over all wavevectors $\vec{k}$ from the first Brillouin zone.
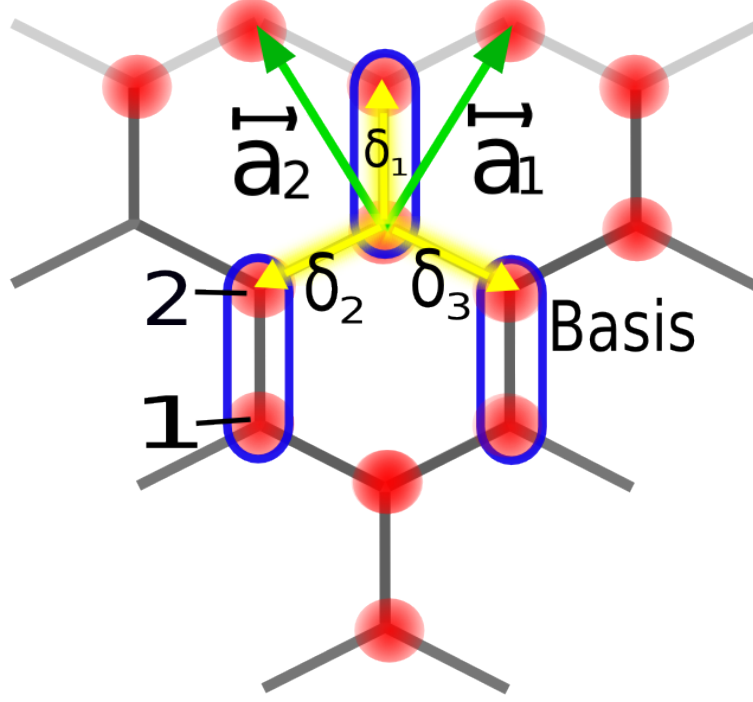
Figure 8: Description of graphene lattice. The two atoms of the Basis are denoted by 1 and 2. An electron of atom 1 (middle Basis) can hop to the atom 2 at the same lattice site ($\vec{\delta}_1$ and to atom 2 of the lower right ($\vec{\delta}_2$), lower left site ($\vec{\delta}_3$) respectively. The yellow lines indicate the hopping of this lattice site

The full Hamiltonian (15) now has the simplified form (24), but the diagonalization procedure is still left.

$$\mathcal{H} = \mathcal{H}_0 - \mathcal{H}_{Hop} = \sum_{\vec{k} \in 1.B.Z.} \left(\hat{a}^\dagger_{\vec{k}}, \hat{b}^\dagger_{\vec{k}} \right) \begin{pmatrix} \epsilon_0 & \phi(\vec{k}) \\ \phi^*(\vec{k}) & \epsilon_0 \end{pmatrix} \begin{pmatrix} \hat{a}_{\vec{k}} \\ \hat{b}_{\vec{k}} \end{pmatrix} \qquad (24)$$

$$\phi(\vec{k}) = -te^{i\vec{k}\vec{\delta}_1} \left(1 + e^{i\vec{k}(\vec{\delta}_2 - \vec{\delta}_1)} + e^{i\vec{k}(\vec{\delta}_3 - \vec{\delta}_1)} \right) \qquad (25)$$

In figure(8) one can easily see that $\vec{\delta}_1 - \vec{\delta}_2 = \vec{a}_1$ and $\vec{\delta}_1 - \vec{\delta}_3 = \vec{a}_2$. Diagonalizing the matrix yields the dispersionrelation $\epsilon(\vec{k})$

$$\epsilon(\vec{k}) = \epsilon_0 \pm \sqrt{\phi(\vec{k})\phi^*(\vec{k})}$$

$$\epsilon(\vec{k}) = \epsilon_0 \pm t\sqrt{3 + 2\cos(k_1 a_0) + 2\cos(k_2 a_0) + 2\cos((k_1 - k_2)a_0)} \qquad (26)$$

The constant energy shift ϵ_0 is not important for the properties discussed later, and will be omitted. Figure(9) shows the dispersion relation of graphene. At this point one should state that the coefficients k_1 and k_2 are not given with respect to
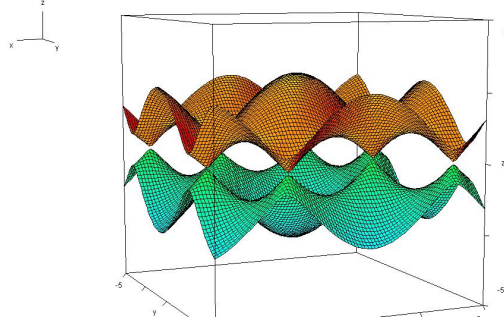
Figure 9: Dispersionrelation of graphene. In the vicinity of the points where the two bands meet each other the charge carriers behave like massless dirac fermions in 2 dimensions.

an orthogonal basis, but to a basis spanned by $\vec{G}_1$ and $\vec{G}_2$. The reciprocal lattice vectors which are taken as basis vectors in equation(21) are neither orthogonal nor normalized fig.(10), but they are linearly independent. We will straighten this deficiency in section(3.3) out when it is necessary.

In the literature, the zeros of equation(26), with $\epsilon_0 = 0$, are often referred to as the Dirac points or K-points.
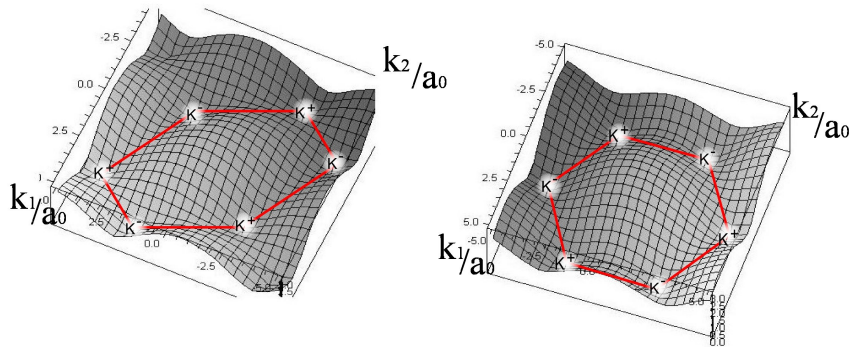
Figure 10: The hexagonal Brillouin zone of the honeycomb lattice and the dispersion relation (shaded, corrugated region). The first one (l) is represented in the non orthogonal basis used in equation(26). The corner points are called K-points. There is always a pair of neighbouring points K^+ and K^- which are inequivalent, i.e. can not be connected by a reciprocal vector.

Figure(10) shows a Brillouin zone with K-points. Some of them can be connected by a vector of the reciprocal lattice, but not all of them. Therefore, the neighbouring K-points are not equivalent and must be both taken into account, in the reduced zone scheme.

21

Equation(24) already suggested a more compact notation:

$$\mathcal{H} = \sum_{\vec{k},\sigma} \left(\hat{a}^{\dagger}_{\vec{k},\sigma}, \hat{b}^{\dagger}_{\vec{k},\sigma} \right) \underbrace{\begin{pmatrix} 0 & \phi(\vec{k}) \\ \phi^*(\vec{k}) & 0 \end{pmatrix}}_{\mathbf{H_0}} \begin{pmatrix} \hat{a}_{\vec{k},\sigma} \\ \hat{b}_{\vec{k},\sigma} \end{pmatrix} = \sum_{\vec{k},\sigma} \boldsymbol{\Upsilon}^{\dagger}_{\sigma}(\vec{k}) \mathbf{H_0} \boldsymbol{\Upsilon}_{\sigma}(\vec{k}) \qquad (27)$$

In (27) above, we introduced the two component Spinor notation with the sub-lattice annihilation operators as its entries. Furthermore we reintroduced the spin σ and we omitted ϵ_0. This form will help us a little bit in our symmetry considerations, moreover it is essential in deriving the Dirac like form of the low energy regime.

3.2 Stability of the K-point

The tight-binding approximation with nearest neighbour hopping used above may be an oversimplified method to calculate the bandstructure of graphene. As we will see, this point of view is not totally right. One of the most fascinating properties of graphene is that the quasi particles exhibit a Dirac like spectrum of ultra relativistic massless particles in the vicinity of the K points. In the following, it will be shown that eigenstates with zero energy are robust against next and third neighbour hopping.
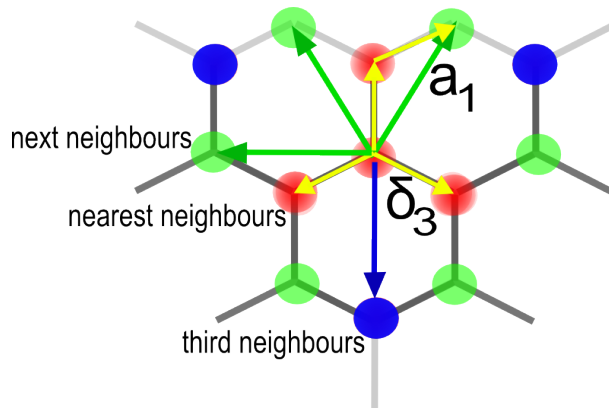
Figure 11: nearest neighbours include a distance of δ_i, next neighbours are connected by a lattice vector and third neighbour hopping

To begin with the next neighbour hopping, we introduce a new term in equation(27). We denote the distance of neighbouring lattice sites again by δ_i.

$$\mathcal{H} = \mathcal{H}_{<n.n.>} - t_{next} \sum_{\vec{n},\sigma} \left(\hat{a}^{\dagger}_{\vec{n},\sigma} a_{\vec{n}+\vec{a}_1-\vec{a}_2,\sigma} + \hat{b}^{\dagger}_{\vec{n},\sigma} b_{\vec{n}+\vec{a}_1-\vec{a}_2,\sigma} + \dots \right) \qquad (28)$$

Figure(11) shows that next neighbours are connected by a lattice vector. Hence next neighbours give diagonal contributions which can be absorbed in ϵ_0 and do not change our spectrum qualitatively.

The third neighbour hopping mixes again creation and annihilation operators of different sublattices.

$$\mathcal{H} = \mathcal{H}_{<n.n.>} - t' \sum_{\vec{n},\sigma} \left(\hat{a}_{\vec{n},\sigma}^\dagger \hat{b}_{\vec{n}-2\delta_1,\sigma} + \hat{a}_{\vec{n},\sigma}^\dagger \hat{b}_{\vec{n}-\delta_1-\delta_2+\delta_3,\sigma} + \hat{a}_{\vec{n},\sigma}^\dagger \hat{b}_{\vec{n}-\delta_1+\delta_2-\delta_3,\sigma} + c.c \right) \tag{29}$$

Now we use the Fourier decomposition of our operators, equation(22). In the same way as it was done in equation(27) we write the Hamiltonian above as a sum of a matrix product of two spinors $\mathbf{\Upsilon}_\sigma$, $\mathbf{\Upsilon}_\sigma^\dagger$ with a matrix $\mathbf{H}_0$. This matrix $\mathbf{H}_0$ contains again only off-diagonal terms $\phi(\vec{k})$, $\phi^*(\vec{k})$.

In order to show that the K-points are stable against other hopping terms, we demonstrate in the following that for certain values of the third neighbour hopping amplitude t', $\phi(\vec{k})$ can still be zero. The modulus of $\phi(\vec{k})$ enters the dispersion relation as shown in section(3.1) and is responsible for the Dirac points. Next we evaluate the nearest and third neighbour terms in the Fourier decomposition.

$$\phi(\vec{k}) = -t \underbrace{\left(e^{i\vec{k}\vec{\delta}_1} + e^{i\vec{k}\vec{\delta}_2} + e^{i\vec{k}\vec{\delta}_3} \right)}_{n.n.} -t' \underbrace{\left(e^{-i2\vec{k}\vec{\delta}_1} + e^{i\vec{k}(\vec{\delta}_1-\vec{\delta}_2+\vec{\delta}_3)} + e^{i\vec{k}(\vec{\delta}_1+\vec{\delta}_2-\vec{\delta}_3)} \right)}_{next-neigh.} \tag{30}$$

As indicated, the first term comes from nearest neighbour hopping and the second is due to third neighbour hopping.

For simplicity, we will proof the claim only for the $e^{i2\vec{k}\vec{\delta}_1}$ third neighbour hopping term in eq.(30) and only give a short statement why it works as well with the others.

$$\phi(\vec{k}) = -te^{i\vec{k}\vec{\delta}_1} \left[1 + e^{-i\vec{k}\vec{a}_2} + e^{-i\vec{k}\vec{a}_1} + \frac{t'}{t} e^{-i3\vec{k}\vec{\delta}_1} \right]$$

Figure(11) shows that lattice vectors and vectors between sites are connected by $\vec{\delta}_1 - \vec{\delta}_2 = \vec{a}_1$ and $\vec{\delta}_1 - \vec{\delta}_3 = \vec{a}_2$.

$$\phi(\vec{k}) = -te^{i\vec{k}\vec{\delta}_1} \left[1 + e^{-i\vec{k}\vec{a}_2} + e^{-i\vec{k}\vec{a}_2} \left(1 + \frac{t'}{t} e^{i\vec{k}\vec{a}_2} \right) \right] = -te^{i\vec{k}\vec{\delta}_1} \tilde{\phi}(\vec{k}) \tag{31}$$

For a certain proportion of t'/t there should be $\vec{k}$ with $\tilde{\phi}(\vec{k}) = 0$ in order to have K-points. We rewrite $\tilde{\phi}(\vec{k})$.

$$\tilde{\phi}(\vec{k}) = 1 + e^{-i\vec{k}\vec{a}_2} + r\left(\frac{t'}{t}\right) e^{i\vec{k}\vec{a}_2+i\varphi} e^{-i\vec{k}\vec{a}_1} \tag{32}$$

with $r(t'/t) = \sqrt{1 + 2\left(\frac{t'}{t}\right) cos(\vec{k}\vec{a}_2) + \left(\frac{t'}{t}\right)^2}$

If we fix $\vec{k}\vec{a}_2$ and let $\vec{k}\vec{a}_1$ vary, then equation(32) has a geometrical interpretation
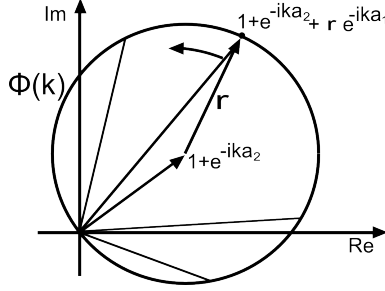
Figure 12: shows equation(32) in geometrical way. We get Dirac points when the energy is zero, i.e. when $|\phi(\vec{k})| = 0$.

as a circle of radius $r\left(\frac{t'}{t}\right)$ with center $1 + e^{-i\vec{k}\vec{a}_2}$ (figure(12)). When the circle hits the origin then Dirac points are possible, i.e. the modulus of $\tilde{\phi}(\vec{k})$ can be zero. This is guaranteed for

$$\frac{t'}{t} = -cos(\vec{k}\vec{a}_2) \pm \sqrt{cos^2(\vec{k}\vec{a}_2) + 1 + 2cos(\vec{k}\vec{a}_2)} \tag{33}$$

Therefore t'/t is either 1 or $-1 - 2cos(\vec{k}\vec{a}_2)$. For $\vec{k}\vec{a}_2 \in (-\pi, \pi)$ the latter yields

$$-3 \leq \frac{t'}{t} < 1 \tag{34}$$

In the case of the remaining two hopping possibilities in equation(30) one gets similar terms leading to the same condition on t'/t. If we would have taken the last term of the third neighbours part in equation(30) instead of the first, we would have gotten

$$\phi(\vec{k}) = -te^{i\vec{k}\vec{\delta}_1}\left(1 + e^{-i\vec{k}\vec{a}_2} + e^{-i\vec{k}\vec{a}_1} + \frac{t'}{t}e^{i\vec{k}(\vec{a}_2 - \vec{a}_1)}\right)$$

Just to complete the discussion we give the result with the second term:

$$\phi(\vec{k}) = -te^{i\vec{k}\vec{\delta}_1}\left(1 + e^{-i\vec{k}\vec{a}_2} + e^{-i\vec{k}\vec{a}_1} + \frac{t'}{t}e^{i\vec{k}(\vec{a}_1 - \vec{a}_2)}\right)$$

Obviously these equations lead to the same constrain(34) for t'/t. As a conclusion of this discussion we found that the Dirac point is stable against additional hopping terms. The hopping amplitude is proportional to the overlapp of wavefunctions between two lattice sites, hence we showed that Dirac points are robust with respect to slight deformations of the lattice. Finally, this part showed, that the honeycomb lattice itself is not solely responsible for massless Dirac fermions but rather a generic class of two dimensional lattices with two atomic basis [8]. Besides hopping terms with certain amplitudes t', vanishing Dirac points come

along with generation of a finite Dirac mass. For instance, a differnce of the sublattices A and B is represented by an additional diagonal term:

$$\mathcal{H} = \mathcal{H}_0 + \underbrace{\sum_{\vec{k},\sigma} \mathbf{\Upsilon}_\sigma^\dagger(\vec{k})\mathbf{H}_1\mathbf{\Upsilon}_\sigma(\vec{k})}_{\mathcal{H}_1}, \qquad \mathbf{H}_1 = \begin{pmatrix} m_A & 0 \\ 0 & m_B \end{pmatrix} \qquad (35)$$

$\mathcal{H}_1$ can be rewritten in terms of Pauli matrices[11] τ_0, τ_3 and the masses $m_+ = (m_A + m_B)/2$ and $m_- = (m_A - m_B)/2$.

$$\mathcal{H}_1 = \sum_{\vec{k},\sigma} \mathbf{\Upsilon}_\sigma^\dagger(\vec{k})\left(m_+\tau_0 - m_-\tau_3\right)\mathbf{\Upsilon}_\sigma(\vec{k}) \qquad (36)$$

The m_+ term can be absorbed in ϵ_0 and does not change anything, the second term m_- has a different sign for A and B sublattice and changes the spectrum from massless particles to particles with finite masses: $\epsilon(\vec{k}) = \pm\sqrt{m_-^2 + |\phi|^2}$. The two dimensional crystal boron nitride exhibits such a sublattice difference because of the distinguishable atoms in the basis B and N. Hence the dispersion relation of BN has no Dirac point and no massless quasiparticles. But the low energy regime of BN is still governed by ultra relativistic quasi particles, in this case, with finite masses.

3.3 QED_{2+1} - Massless Dirac Particles in Graphene

Starting from the tight-binding Hamiltonian in equation(24) we will develop the low-energy approximation in the following part. One might have already noticed that in figure(9) the dispersion relation is linear near the points where the two bands touch each other and momenta are small.

At first, it is important to express the coefficients k_1 and k_2 in an orthonormal basis

$$e_1 = \begin{pmatrix} 1 \\ 0 \end{pmatrix}, \qquad e_2 = \begin{pmatrix} 1 \\ 0 \end{pmatrix}$$

In this basis the coefficients become

$$k_1 = \frac{\sqrt{3}\kappa_1 + \kappa_2}{2}, \qquad k_2 = \frac{\sqrt{3}\kappa_1 - \kappa_2}{2} \qquad (37)$$

According to eq.(37) our dispersion relation changes and gains the full hexagonal symmetry as shown in figure)10:

$$\epsilon(\vec{k}) = \sqrt{3 + 2\cos\left(a_0\frac{\sqrt{3}\kappa_1 + \kappa_2}{2}\right) + 2\cos\left(a_0\frac{\sqrt{3}\kappa_1 - \kappa_2}{2}\right) + 2\cos(\kappa_2 a_0)} \qquad (38)$$

---

[11] $\tau_0 = \begin{pmatrix} 1 & 0 \\ 0 & 1 \end{pmatrix}$, $\tau_1 = \begin{pmatrix} 0 & 1 \\ 1 & 0 \end{pmatrix}$, $\tau_2 = \begin{pmatrix} 0 & -i \\ i & 0 \end{pmatrix}$ and $\tau_3 = \begin{pmatrix} 1 & 0 \\ 0 & -1 \end{pmatrix}$

The K-points where (38) is zero are the six points:

$$K^- = \frac{4\pi}{3a_0}\begin{pmatrix} 0 \\ 1 \end{pmatrix}, \qquad \frac{4\pi}{3a_0}\begin{pmatrix} \sqrt{3}/2 \\ -1/2 \end{pmatrix}, \qquad \frac{4\pi}{3a_0}\begin{pmatrix} -\sqrt{3}/2 \\ -1/2 \end{pmatrix} \qquad (39)$$

$$K^+ = \frac{4\pi}{3a_0}\begin{pmatrix} 0 \\ -1 \end{pmatrix}, \qquad \frac{4\pi}{3a_0}\begin{pmatrix} \sqrt{3}/2 \\ 1/2 \end{pmatrix}, \qquad \frac{4\pi}{3a_0}\begin{pmatrix} -\sqrt{3}/2 \\ 1/2 \end{pmatrix}$$

We take two neighbouring inequivalent K-points and denote them with K^+ and K^- in the following (figure(13)). Furthermore we expand the tight-binding Hamiltonian eq.(27) to the first order in $\vec{\kappa}$ or shrink the lattice spacing $a_0 \to 0$ which is a continuum approximation. The k - dependence of the tight-binding Hamiltonian is represented by the $2x2$-matrix $\mathbf{H}_0$ which depends in turn on $\phi(\vec{k})$.

$$\phi(\vec{k}) = -t\left(e^{i\frac{a_0}{3}\kappa_2} + e^{ia_0(5/6\kappa_2-\sqrt{3}/2\kappa_1)} + e^{-ia_0(\sqrt{3}/2\kappa_1-1/6\kappa_2)} \right) \qquad (40)$$

$$\phi(\vec{k}) = \phi(\vec{K}^\pm + \vec{p}) \approx \phi(K^\pm) + \begin{pmatrix} \partial_1\phi(\vec{k}) \\ \partial_2\phi(\vec{k}) \end{pmatrix} \cdot \begin{pmatrix} p_1 \\ p_2 \end{pmatrix}$$

$$\Rightarrow \phi_{K\pm}(\vec{p}) = \pm\hbar v_F(p_1 \mp ip_2)$$

In the last line of equation(41) we introduced the Fermi velocity $v_F \sim ta_0/\hbar \approx 10^6 \frac{m}{s}$ [?] [19]. According to [?] the hopping amplitude is $t = 2.3eV$ and the lattice spacing $a_0 = 2.46$ Angstroem.
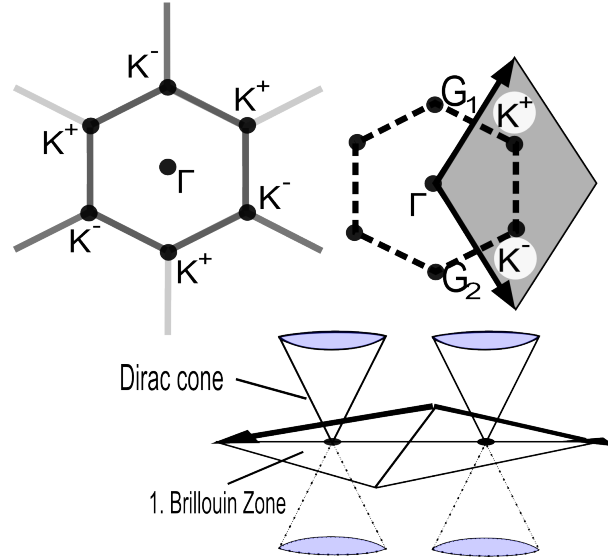

Figure 13: Two equivalent first Brillouin zones (upper right+left), both containing the same area. The left has two K-points K^+ and K^- lying in the interior. (lower right) linearized dispersion relation in the first Brillouine Zone.

Due to the small momenta expansion we replace the sum over wavevectors in eq.(27) of the first Brillouine zone (1.BZ) by an integral over the Dirac cone (DC).

$$\sum_{\vec{k}\in 1.BZ} \rightarrow \frac{(2\pi)^2}{S} \int_{DC} \frac{d^2p}{(2\pi)^2}$$

$S = \sqrt{3}\frac{a_0^2}{2}$ is the area of a unit cell.

At this step there are two crucial points. The first one is that in contrast to the real dispersionrelation the effective one grows up to infinity. Hence we need a proper energy cutoff which preserves the number of states, that is according to [8]:

$$\hbar v_F \sqrt{\frac{(2\pi)^2/S}{2\pi}} = \frac{\hbar v_F}{a_0}\sqrt{\frac{4\pi}{\sqrt{3}}} \approx 2.33t$$

Moreover we have to take both K-points into account. Figure(13) shows the two cones in the first Brillouine zone. A low energy expansion hits of course both. Finally we are able to build the low energy Hamiltonian of graphene

$$\mathcal{H}_0 = \frac{(2\pi)^2}{S} \sum_\sigma \int_{1.BZ} \frac{d^2k}{(2\pi)^2} \mathbf{\Upsilon}_\sigma^\dagger(\vec{k})\mathbf{H}_0\mathbf{\Upsilon}_\sigma(\vec{k})$$

$$\approx \sum_\sigma \int_{DC} \frac{d^2p}{(2\pi)^2} \left[\mathbf{\Upsilon}_\sigma^\dagger(\vec{K}^+ + \vec{p}) \underbrace{\begin{pmatrix} 0 & \hbar v_F(p_1 - ip_2) \\ \hbar v_F(p_1 + ip_2) & 0 \end{pmatrix}}_{\mathbf{H}_{K+}(\vec{p})} \mathbf{\Upsilon}_\sigma(\vec{K}^+ + \vec{p}) \right] \quad (41)$$

$$+ \sum_\sigma \int_{DC} \frac{d^2p}{(2\pi)^2} \left[\mathbf{\Upsilon}_\sigma^\dagger(\vec{K}^- + \vec{p}) \underbrace{\begin{pmatrix} 0 & -\hbar v_F(p_1 + ip_2) \\ -\hbar v_F(p_1 - ip_2) & 0 \end{pmatrix}}_{\mathbf{H}_{K-}(\vec{p})} \mathbf{\Upsilon}_\sigma(\vec{K}^- + \vec{p}) \right]$$

In view of a QED like description we introduce the four component spinor $\Psi_\sigma(\vec{p})$.

$$\Psi_\sigma(\vec{p}) = \begin{pmatrix} \psi_{K^+,\sigma}(\vec{p}) \\ \psi_{K^-,\sigma}(\vec{p}) \end{pmatrix} = \begin{pmatrix} \hat{a}_\sigma(\vec{K}^+ + \vec{p}) \\ \hat{b}_\sigma(\vec{K}^+ + \vec{p}) \\ \hat{b}_\sigma(\vec{K}^- + \vec{p}) \\ \hat{a}_\sigma(\vec{K}^- + \vec{p}) \end{pmatrix} \quad (42)$$

In (42), the sublattice dependence of the 2-spinor $\Psi_{K^-,\sigma}$ of the K^- point is swapped, compared to that of $\Psi_{K^+,\sigma}$ at K^+. But this is a small price compared to

the easier notation that we gain for the 2×2 matrices in equation(42): $\mathbf{H}_{K\pm}(\vec{p}) = \pm\hbar v_F(\tau^1 p_1 + \tau^2 p_2)$. The τ^i denote the Pauli matrices. Moreover the fact that the two distinguishable K-points give another quantum number additional to the sublattice. Now we rewrite $\mathcal{H}_0$ with equation(42)

$$\mathcal{H}_0 = \hbar v_F \sum_\sigma \int_{DC} \frac{d^2p}{(2\pi)^2} \Psi_\sigma^\dagger(\vec{p}) \underbrace{\begin{pmatrix} 0 & p_1 - ip_2 & 0 & 0 \\ p_1 + ip_2 & 0 & 0 & 0 \\ 0 & 0 & 0 & -p_1 + ip_2 \\ 0 & 0 & -p_1 - ip_2 & 0 \end{pmatrix}}_{\mathbf{H}_0(\vec{p})} \Psi_\sigma(\vec{p})$$

$$(43)$$

The matrix $\mathbf{H}_0(\vec{p})$ in equation(43) almost looks like one of the α matrices which we define as[12]

$$\alpha^i = \tilde{\tau}^3 \otimes \tau^i = \begin{pmatrix} \tau_i & 0 \\ 0 & -\tau^i \end{pmatrix} \tag{44}$$

The tilde $\tilde{\tau}^3$ indicates the action upon the K-point degree of freedom whereas τ^i are responsible for the sublattice pseudospin. The α^i matrices fulfil the Clifford algebra

$$\{\alpha^i, \alpha^j\} = 2\delta^{ij}\mathbf{1} \tag{45}$$

The introduction of α matrices allows a real compact notation for $\mathbf{H}_0(\vec{p})$ (43):
$\mathbf{H}_0(\vec{p}) = \alpha^1 p_1 + \alpha^2 p_2$
However we have not yet reached our goal of a QED description of graphene. Thus we will spend more time in changing our notation for Hamiltonians. The reader should not be confused, everything is just for the purpose of getting as near as possible to relativistic quantum theory.
Hence, we introduce once more new matrices, the so called γ-matrices.

$$\gamma^0 = \beta = \tilde{\tau}^1 \otimes \mathbf{1}_2 = \begin{pmatrix} 0 & \mathbf{1}_2 \\ \mathbf{1}_2 & 0 \end{pmatrix}, \qquad \gamma^\alpha = \beta\alpha^\alpha = \begin{pmatrix} 0 & \tau^\alpha \\ -\tau^\alpha & 0 \end{pmatrix}$$

$$\gamma^5 = i\gamma^0\gamma^1\gamma^2\gamma^3 = \begin{pmatrix} \mathbf{1}_2 & 0 \\ 0 & -\mathbf{1}_2 \end{pmatrix} \tag{46}$$

This is also known as the Weyl or chiral representation[13] of γ matrices. The γ^5-matrix will be important for us because spinors with a definite chirality in relativistic quantum mechanics are eigenstates of γ^5. In the next section we will discuss similarities and differences between the low energy threoy of graphene

---

[12]These are not the α matrices from the usual Dirac operator. In books on relativistic quantum mechanics one would find $\alpha = \begin{pmatrix} 0 & \sigma \\ \sigma & 0 \end{pmatrix}$ and $\beta = \begin{pmatrix} 1 & 0 \\ 0 & -1 \end{pmatrix}$

[13]This is a commonly used representation in the case of massless fermions. It differs with the usual definition: $\gamma^0 = \begin{pmatrix} 1 & 0 \\ 0 & -1 \end{pmatrix}$, $\gamma^i = \begin{pmatrix} 0 & \sigma^i \\ -\sigma^i & 0 \end{pmatrix}$ and $\gamma^5 = \begin{pmatrix} 0 & 1 \\ 1 & 0 \end{pmatrix}$

and the high energy description of neutrinos.

The γ matrices fulfil the usual anti-commutation relations

$$\{\gamma^\mu, \gamma^\nu\} = 2g^{\mu\nu}\mathbf{1}_4, \qquad g^{\mu\nu} = diag(1, -1, -1, -1), \qquad \mu, \nu = 0, 1, 2, 3 \quad (47)$$

The Dirac equation exhibits not adjoint spinors $\psi^\dagger$ but slashed spinors $\bar{\Psi}_{sigma} = \Psi_\sigma^\dagger(\vec{p})\gamma^0$

Finally, the Hamiltonian has the form:

$$\mathcal{H}_0 = -\sum_\sigma \int_{DC} \frac{d^2p}{(2\pi)^2} \bar{\Psi}_\sigma(\vec{p}) \underbrace{\hbar v_F(\gamma^1 p_1 + \gamma^2 p_2)}_{\mathbf{H}_0^D(\vec{p}) = \gamma^0 \mathbf{H}(\vec{p})} \Psi_\sigma(\vec{p}) = -\sum_\sigma \int_{DC} \frac{d^2p}{(2\pi)^2} \bar{\Psi}_\sigma(\vec{p}) E(\vec{p}) \Psi \sigma(\vec{p})$$

$$(48)$$

$$\mathcal{H}_0 = -\hbar v_F \sum_\sigma \int_{DC} \frac{d^2p}{(2\pi)^2} \bar{\Psi}_\sigma(\vec{p}) \begin{pmatrix} 0 & 0 & 0 & -p_1 + ip_2 \\ 0 & 0 & -p_1 - ip_2 & 0 \\ 0 & p_1 - ip_2 & 0 & 0 \\ p_1 + ip_2 & 0 & 0 & 0 \end{pmatrix} \Psi_\sigma(\vec{p})$$

To complete our journey from condensed matter to relativistic quantum mechanics we will couple our quasi particles to electromagnetic fields and derive the Lagrangian $\mathcal{L}$. Furthermore we transform equation(48) back to $\vec{r}$-space and use the canonical representation of wavevectors $p_k \to -i\partial_k$ and energy $E \to i\partial_t$:

$$\mathcal{H}_0 = \sum_\sigma \bar{\Psi}_\sigma(t, \vec{r}) \left[-i\hbar v_F(\gamma^1 \partial_1 + \gamma^2 \partial_2)\right] \Psi_\sigma(t, \vec{r}) = i\hbar \sum_\sigma \bar{\Psi}_\sigma \gamma^0 \partial_t \Psi \quad (49)$$

Where the Fourier transform of spinors was used:

$$\int \frac{d^2p}{(2\pi)^2} \mathcal{F}\Psi(\vec{p})\mathcal{F}^{-1} = \int \frac{d^2r'}{(2\pi)^2} \int \frac{d^2p}{(2\pi)^2} \Psi e^{\vec{p}(\vec{r}-\vec{r}')} = \Psi(\vec{r}) \quad (50)$$

The electromagnetic field can be introduced by minimal coupling to the momentum:

$$\vec{p} \to \vec{p} - \frac{e}{c}\vec{A} = -i\hbar\left(\partial_{\vec{r}} + \frac{ie}{\hbar c}\vec{A}\right) = -i\hbar\vec{D}$$

Here and through out the whole text, the convention is used where $e = -1.6 \cdot 10^{-19} As$, $\vec{A}$ is the vector potential. In the last step we defined the covariant derivativ.

From quantum electrodynamics, we know how to get from the Lagrangian $\mathcal{L}$ to the Hamiltonian $\mathcal{H}$ [25]. Starting from $\mathcal{L}$, the conjugated momenta to Ψ_α are $\pi_\alpha = \frac{\partial \mathcal{L}}{\partial \dot{\Psi}_\alpha} = i\Psi_\alpha^\dagger$. By applying a Legendre transform to $\mathcal{L}$ one gets $\mathcal{H}$. We do it here the other way round. The Langrangian of quasi-particles in graphene which

do not interact with each other but do interact with the electromagnetic field has the form:

$$\mathcal{L} = \sum_{\sigma} \bar{\Psi}_{\sigma}(t,\vec{r}) \left[i\gamma^0(\hbar\partial_t - i\mu_\sigma) - i\hbar v_F \gamma^\alpha D_\alpha \right] \Psi_\sigma(t,\vec{r}) \qquad (51)$$

Because we are still in the non-relativistic regime, only the description looks like a relativistic one, the Zeeman term μ_σ must be included in (51). Apart from the Zeeman term equation(51) looks like the QED Lagrangian for massless fermions in an electromagnetic field:

$$\mathcal{L} = \bar{\Psi}(i\hbar\gamma^\mu D_\mu)\Psi \qquad (52)$$

Besides graphene, there is another condensed matter system with a QED_{2+1} description, a d-wave superconductor. But that model has a different coupling to the magnetic field due to supercurrents [8].

3.4 QED_{2+1} quasi-particles versus QED_{3+1} neutrinos

So far we have tried to work out similarities to quantum electrodynamics(QED), now we will see what differences there are.
At first, we introduce the helicity operator

$$h(\hat{k}) = \frac{\boldsymbol{\Sigma} \cdot \vec{k}}{|\vec{k}|}; \qquad \boldsymbol{\Sigma} = \begin{pmatrix} \vec{\sigma} & 0 \\ 0 & \vec{\sigma} \end{pmatrix} \qquad (53)$$

$\boldsymbol{\Sigma}$ acts on the spin degrees of freedom, $\vec{\sigma}$ is an array of Pauli matrices and $\vec{k}$ is the wavevector. Helicity is the projection of the spin onto the direction of motion. Because of $(\sigma^i)^2 = \mathbf{1}$, $h(\vec{k})^2 = 1$ and the eigenvalues of the helicity operator are ± 1. One distinguishes the eigenstates by:

- $+1$ right handed particles, spin is parallel to the momentum $\vec{k}$

- -1 left handed particles, spin points in the opposite direction of $\vec{k}$

Secondly, we will derivate a proper form of the Dirac equation with zero restmass, where helicity directly appears.

$$\tilde{\gamma}^\mu k_\mu \Psi = 0 \qquad (54)$$

The tilde above the Dirac matrices $\tilde{\gamma}^\mu$ indicates, that we are using the standard notation of the gamma matrices.

$$\tilde{\gamma}^0 = \begin{pmatrix} \mathbf{1} & 0 \\ 0 & -\mathbf{1} \end{pmatrix}, \qquad \tilde{\gamma}^i = \begin{pmatrix} 0 & \sigma^i \\ \sigma^i & 0 \end{pmatrix} \qquad (55)$$

Later we will introduce the chiral representation to compare it to the low energy theory of graphene. We multiply (54) with $\gamma^5\gamma^0 = -i\gamma^1\gamma^2\gamma^3$ from the right. By using the anti commutation properties of the Dirac matrices $\{\gamma^\mu, \gamma^\nu\} = 2g^{\mu\nu}\mathbf{1}$ we get

$$(\gamma^5 k_0 - k_i \Sigma^i)\Psi = 0 \tag{56}$$
$$\Rightarrow \mathbf{\Sigma} \cdot \vec{k}\Psi = k_0 \tilde{\gamma}^5 \Psi$$

Next we plug in plane waves for positive and negative energies respectively in eq.(57):

$$\Psi_{E+}(x^\alpha) = e^{-ik^\alpha x_\alpha}\Psi(k^\alpha) = e^{-i(k^0 x_0 - \vec{k}\vec{x})}\Psi(k^\alpha) \tag{57}$$
$$\Psi_{E-}(x^\alpha) = e^{ik^\alpha x_\alpha}\Psi(k^\alpha) = e^{i(k^0 x_0 - \vec{k}\vec{x})}\Psi(k^\alpha) \tag{58}$$

Because of equation(54) and $\tilde{\gamma}^\nu k_\nu \tilde{\gamma}^\mu k_\mu \Psi = 0$, $k^\alpha k_\alpha = 0$. Hence $k^0 = E = |\vec{k}|$ and in equation(57) the helicity operator appears

$$\frac{\mathbf{\Sigma} \cdot \vec{k}}{|\vec{k}|}\Psi(k^\alpha) = h(\vec{k})\Psi(k^\alpha) = \pm\tilde{\gamma}^5 \Psi(k^\alpha) \tag{59}$$

The $\tilde{\gamma}^5$ operator is called chirality operator. The last equation shows that eigenstates of the helicity operator are states with a definite chirality. Instead of solving equation(59) we switch our Dirac matrices from the standard representation to the chiral representation.

$$U = \frac{1}{2}(\mathbf{1} + \tilde{\gamma}^5) \tag{60}$$

U defines a unitary transformation to the chiral representation:

$$\Psi \rightarrow \Psi^{ch} = U^\dagger\Psi; \qquad \gamma^\mu = U^\dagger\gamma^\mu U \tag{61}$$

$$\gamma^{0,ch} = -\tilde{\gamma} = \begin{pmatrix} 0 & -\mathbf{1} \\ -\mathbf{1} & 0 \end{pmatrix}, \qquad \gamma^k = \tilde{\gamma}^k = \begin{pmatrix} 0 & -\sigma^k \\ \sigma^k & 0 \end{pmatrix} \tag{62}$$

$$\gamma^5 = \tilde{\gamma}^5 = \begin{pmatrix} \mathbf{1} & 0 \\ 0 & -\mathbf{1} \end{pmatrix}$$

The γ^5 matrix is diagonal in this representation, this suggests itself the name, chiral representation. Therefore we can split the spinor Ψ into two subspinors of definite chirality.

$$\Psi^{ch} = \begin{pmatrix} \psi_1 \\ \psi_2 \end{pmatrix} \tag{63}$$

We use these relations to transform the Dirac equation into the chiral representation:

$$(-i\hbar\tilde{\gamma}^\mu\partial_\mu + m)\Psi = 0 \tag{64}$$
$$U^\dagger(-i\hbar\tilde{\gamma}^\mu\partial_\mu + m)UU^\dagger\Psi = 0$$
$$(i\hbar\gamma^{0,ch}\partial_0 - i\hbar\gamma^k\partial_k)\Psi^{ch} - m\mathbf{1}_4\Psi^{ch} = 0$$

If the mass term in the last line of (65) is zero, then the Dirac equation decays into two decoupled equations.

$$(-i\partial_0 + i\sigma^k\partial_k)\psi_2 = 0 \tag{65}$$

$$(-i\partial_0 - i\sigma^k\partial_k)\psi_1 = 0 \tag{66}$$

These two equations are known as the Weyl equations for neutrinos. Only one of the two equations on its own is not parity invariant [24]. To the common knowledge, there are no right handed neutrinos in nature and only eigenstates with negative chirality exist, hence the first equation(65) is the relevant one. We plug in the first equation plane wave solutions of positive and negative energy $\psi_2 = e^{\mp k^\alpha x_\alpha}\phi(k^\alpha)$:

$$\mathbf{\Sigma} \cdot \vec{k}\phi(\vec{k}) = \mp E\phi(\vec{k}) \tag{67}$$

This equation tells us that states of positive energy, i.e. neutrinos ν, exhibit negative chirality and states of negative energy, anti-neutrinos $\bar{\mu}$, have positive helicity. Because massless particles move with the speed of light, we cannot go to a rest frame and change the spin direction as it would be possible for massive particles like electrons. A parity transformation $\mathcal{P}$ changes the direction of momentum $\vec{k} \to -\vec{k}$ leaving the spin unchanged. In this way we can transform a neutrino with negative helicity into one with positive helicity which does not fulfil equation(65) but the, in nature, absent equation(66). Therefore we have no parity invariance for neutrinos. Charge conjugation $\mathcal{C}$ operation connects states with positive and negative chirality [24] and changes the sign of the charge $e \to -e$. Because states with positive chirality are absent in nature, equation(65) on its own violates charge conjugation symmetry. It is known that the combined $\mathcal{CP}$ transformation is preserved.

Until now we have not talked about graphene so we need to catch up that topic. One should not be confused with the fact that we used the second quantized picture in the graphene part and the first quantized picture in the neutrino part. We compare only the structure of the equations. Second and first quantization are just two ways of describing the same thing. $\mathbf{H}_0^D(\vec{p}) = \hbar v_F(\gamma^1 p_1 + \gamma^2 p_2) = E(\vec{p})$ in equation(49) is similar to the last line in (65), but without the mass term. Above it was mentioned that for general honeycomb 2D-crystals like BN and even for graphene there are mass generating mechanisms like differences of the two sublattices.

We have seen that without the mass term, the Dirac equation in the chiral representation decays into two equation that are formulated in the subspace of definite chirality. This is nothing new for us because we constructed the hamiltonian in equation(49) by unifying two 2-component spinors in the subspace of definite valley index to a 4-component spinor:

$$\Psi_\sigma(\vec{p}) = \begin{pmatrix} \psi_{K^+,\sigma}(\vec{p}) \\ \psi_{K^-,\sigma}(\vec{p}) \end{pmatrix} \tag{68}$$

32

In that sense, we can introduce chirality to low energy graphene by talking about the valley index. Positive chirality refers to the K^+-valley and negative chirality to the K^- valley.

The real difference is that we have no τ^3 Pauli matrix in the case of graphene[14]. Therefore $\vec{p}$ lies in a plane and $\vec{\tau} = (\tau^1, \tau^2)$ does not have the meaning of the usual spin operator. Moreover, since τ^3 is the only generator of angular momentum there is no non-abelian Lie algebra that can restrict its possible eigenvalues [8]. All in all we can not construct a helicity operator in the sense of, massless ultra relativistic particles. Of course we can define a pseudo helicity operator

$$h^{2D}(\vec{p}) = \frac{\mathbf{\Sigma} \cdot \vec{p}}{|\vec{p}|}, \qquad \mathbf{\Sigma} = \begin{pmatrix} \vec{\tau} & 0 \\ 0 & \vec{\tau} \end{pmatrix} \tag{69}$$

Furthermore for graphene both Weyl equations (65) and (66) are present. States with positive energy $\hbar v_F |\vec{p}|$ are electrons and states with negative energy are holes. Hence equation(67) describes electrons(e) and holes(h) at the K^- valley.

$$\hbar v_F \mathbf{\Sigma} \cdot \vec{p}\, \psi_{K^-}^{e,h}(\vec{p}) = \mp \hbar v_F |\vec{p}| \psi_{K^-}^{e,h}(\vec{p}) \tag{70}$$
$$\Rightarrow h^{2D}(\vec{p}) \psi_{K^-}^{e}(\vec{p}) = -\psi_{K^-}^{e}(\vec{p})$$
$$\Rightarrow h^{2D}(\vec{p}) \psi_{K^-}^{h}(\vec{p}) = \psi_{K^-}^{h}(\vec{p})$$

At the K^+ - point these relations are just inverted for electron and holes. In total these relations tell us that at a given $K^\pm$ point, the direction of momentum for electrons and holes with the same energy is opposite.

Finally, the conservation of chirality exhibits a nice physical meaning. If transfer of quasiparticles between valleys is suppressed then backward scattering is absent in our system [8]. This is visualised in figure(14). It depends on the type of impurities in the sample [7] whether valley mixing is present or not.

---

[14]τ and σ both are Pauli matrices but the former refers to pseudo spin, i.e. sublattice index, whereas the latter refers to real spin
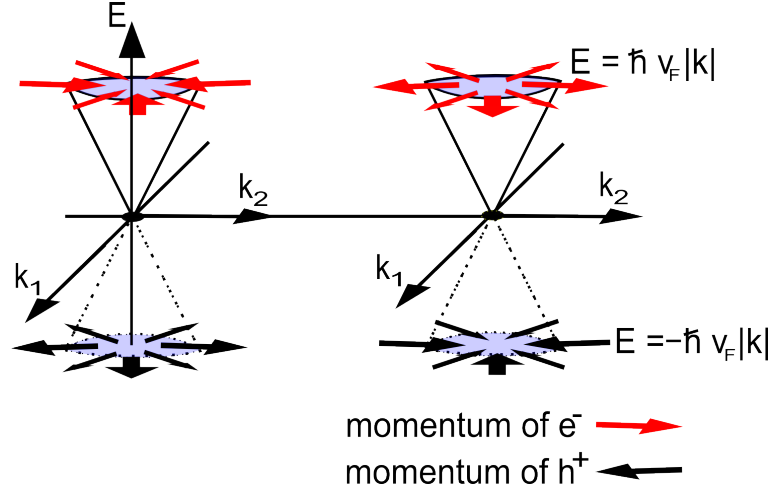
Figure 14: The two Dirac cones at the K^- point (left) and the K^+ point (right). The arrows indicate the direction of motion of electrons and holes respectively. Electrons and holes at each valley have opposite helicity. Conservation of chirality means that states have a definite valley index.

4   The Quantum Hall Effect in Graphene

The rise of micro electronics in the 70ies and 80ies led to a great interest in examinig the two dimension like structures of field effect transistors. In 1980 Klaus von Klitzing and collaborators [12] investigated two dimensional structures in high magnetic fields and discovered a quantized Hall resistance. The quantization of the Hall conductivity in integer multiples of the squared electron charge divided by Planck's constant

$$\sigma_{xy} = \frac{e^2}{h} \cdot n \tag{71}$$

is an absolutely extraordinary phenomenon and from the common sense's point of view, an unexpected feature. Usually, one has to take several material dependent parameters into account in order to calculate transport properties. For instance the effective mass, the density of charge carriers, the dispersion relation, electron interactions or the concentration of impurities heavily influence the conductivity. On the one hand some of these are less relevant for a real two dimensional gas of free fermions appearing in quantum wells or on top of MOSFETs (Metal-oxidized Silicon Field Effect Transistors), but on the other hand it is still amazing in which way these effects play together and reduce just to two fundamental constants, the electroncharge $e = -1.6 \cdot 10^{-19} As$ and Planck's constant $h = 6.626 \cdot 10^{-34} Js$. There are various types of phenomena referred to as the quantum Hall effect (QHE). They exhibit the common observation of Hall conductance quantization $\sigma_{xy} = \frac{e^2}{h} \frac{p}{q}$ where p, q are integers. From the theoretical point of view there are two different quantum Hall effects. Namely, the integer (IQHE) and the fractional
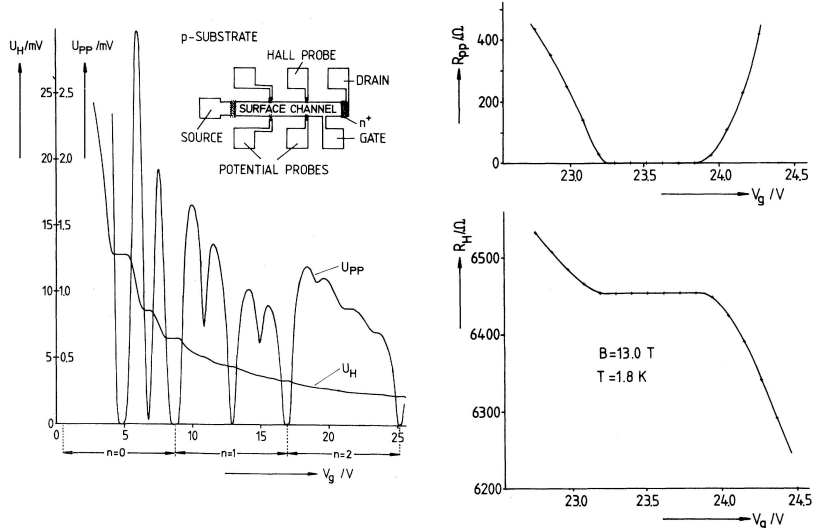
Figure 15: Quantum Hall effect measurements of Klaus von Klitzing, G. Dorda and M. Pepper, PRL Vol.45 No.6 (1980) [12]. (on the left) Hall voltage U_H and longitudinal Voltage U_{PP} as a function of the backgate potential V_g. V_g is proportional to the charge carrier concentration. Inset on the left shows the device with length $L = 400\mu m$ and width $W = 50\mu m$. The two diagramms on the right show the longitudinal resistance (upper right) and the Hall resistance R_H (lower right) at $B = 13T$. One can see the Hall plateau of R_H and the vanishing longitudinal resistance.

quantum Hall effect. The prior can be explained within a framework of non interacting particles whereas the latter can not be explained without electron-electron interactions, in a single particle framework. In the following part only the IQHE will be discussed. First of all, this restriction is because QHE experiments with graphene have not yet advanced to the region where fractional effects become visible and secondly because the fractional quantum Hall effect requires much more advanced methods and tools which would lie clearly out of the scope of this text. Nevertheless, the fractional quantum Hall effect had great influence on theoretical solid state physics and led for example to the theory of composite fermions [9].

4.1   The Hall Effect and Electrons in magnetic Fields

To begin with, we consider the experimental setup given in figure(16). To recapitulate the classical Hall effect, imagine a current density $\vec{j} = en_e\vec{v}$ injected from the right, e is the charge, n_e the charge carrier density and $\vec{v}$ the velocity. There is a potential difference V between 1 and 2 in figure(16) and a perpendicular
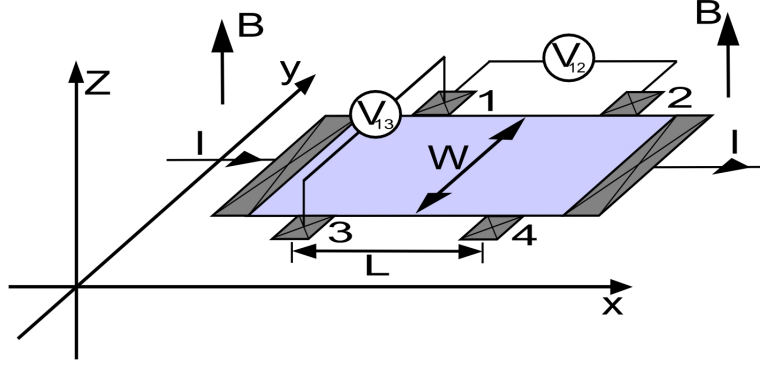
35

Figure 16: Geometry of a typical "Hall Crocodile" used to investigate the QHE. The current flows in the positive x-direction from one lead to the other, a constant magnetic field points in the z-direction. The longitudinal resistance/conductivity is obtained by V_{12} the Hall resistance/conductivity by V_{13}

magnetic field of strength B applied on the sample. Due to the Lorentz force

$$F_L = e \left(E + \frac{1}{c} \cdot [\vec{v} \times B] \right) \tag{72}$$

the current will be forced in the y-direction until there is a counter voltage V_{13} between point 1 and 3 in (16), strong enough to compensate the force of the magnetic field.

$$E_{13} = \frac{V_{13}}{L} = -\frac{v}{c} \cdot B$$

Hence, with Ohm's law $\vec{j} = \sigma \vec{E}$ the Hall resistivity ρ_{xy} is

$$\rho_{xy} = \frac{E_{13}}{j} = \frac{vB}{en_e v} = \frac{B}{en_e c} \tag{73}$$

This is the classical Hall effect, the Hall resistivity depends on the magnetic field, the carrier density and on the sign of the charge. Therefore it can be used to determine the type of charge carrier, electrons or holes.

To prepare a quantum mechanical description of the Hall effect, we will have a look at the electon motion in a magnetic field at first.
We consider a two dimensional problem, we will see later how two dimensional systems are realized. In the case of graphene it is already known, but the materials used here have a purely non-relativistic description.
The Hamiltonian of an electron confined in a plane with a magnetic field has the

following form ([27]p.20).

$$\mathcal{H} = \frac{1}{2m} \underbrace{\left(\vec{p} - e/c\vec{A}(\vec{r})\right)^2}_{\vec{\pi}^2} + g\mu_B s B \qquad (74)$$

The last term in equation(74) is the Zeeman term, $s = \pm\frac{1}{2}$ is the Spin quantum number, $g \approx 2$ is the Landé factor and $\mu_B = \frac{e\hbar}{2mc}$ is the Bohr magneton. This term induces only a spin dependent splitting and will be omitted in the following discussion.

We have a certain freedom to choose the vector potential and there are two convenient ways. The first is the symmetric gauge $\vec{A}(\vec{r}) = \frac{B}{2}(-y, x, 0)$ which is appropriate in an isometric problem. The second one is helpful in a, in one direction, translation invariant system, $\vec{A}(\vec{r}) = B(0, x, 0)$, it is called the Landau gauge. One may check that both choices give the same magnetic field $\vec{B} = \nabla \times \vec{A}$. In our case of an infinite plane the symmetric gauge will be used due to rotational invariance. Due to the vector potential $\vec{A}(\vec{r})$, the canonical momentum operator $\vec{p}$ does not commute with the Hamiltonian although the system is translational invariant. From the Heisenberg equation of motion we get for the velocity operator.

$$\vec{v} = \dot{\vec{r}} = \frac{i}{\hbar}[\mathcal{H}, \vec{r}] = \frac{1}{m}(\vec{p} - e/c\vec{A}(\vec{r})) \qquad (75)$$

So we can define a dynamical momentum operator $\vec{\pi} = (\vec{p} - e/c\vec{A}(\vec{r}))$. The y and x component of $\vec{\pi}$ do not commute with each other:

$$[\pi_x, \pi_y] = i\hbar e/c(\partial_x A_y - \partial_y A_x) = i\hbar e/cB = -i\frac{\hbar^2}{l^2} \qquad (76)$$

$l^2 = \frac{\hbar c}{|e|B}$ is called magnetic length or Larmor radius. As we will see later, this quantity is related to the radius of the cyclotron orbit of the lowest Landau level. Thus, we can treat the two dynamical momenta π_x and π_y as conjugated variables. The Hamiltonian eq.(74) is similar to the well-known harmonic oscillator

$$\mathcal{H} = \frac{1}{m}(\pi_x^2 + \pi_y^2) \qquad (77)$$

We can define creation and annihilation operators

$$\hat{a}^\dagger = \frac{l}{\sqrt{2}\hbar}(\pi_x + i\pi_y) \qquad (78)$$

$$\hat{a} = \frac{l}{\sqrt{2}\hbar}(\pi_x - i\pi_y)$$

and plug them into the Hamiltonian (77). The result is the famous harmonic

oscillator, which allows us to write down all necessary properties immediately.

$$\mathcal{H} = \hbar\omega_c \left(\hat{a}^\dagger a + \frac{1}{2} \right), \qquad \omega_c = \frac{|e|B}{mc} \tag{79}$$

$$E_n = \hbar\omega_c \left(n + \frac{1}{2} \right), \qquad n \in \{0, 1, 2, \ldots\}$$

Next we will write out the whole hamiltonian in the symmetric gauge to derive the total set of eigenstates.

$$\mathcal{H} = \frac{1}{2m} \left[\left(-i\hbar\partial_x + \frac{eB}{c}\frac{y}{2} \right)^2 + \left(-i\hbar\partial_y - \frac{eB}{c}\frac{x}{2} \right)^2 \right] \tag{80}$$

We introduce dimensionless quantities

$$x, y \to \tilde{x} = \frac{x}{l}, \qquad E \to \tilde{E} = \frac{E}{\hbar\omega_c} \tag{81}$$

Rewriting equation(80) gives

$$\mathcal{H} = \frac{1}{2} \left[\left(-i\partial_{\tilde{x}} - \frac{\tilde{y}}{2} \right)^2 + \left(-i\partial_{\tilde{y}} + \frac{\tilde{x}}{2} \right)^2 \right] \tag{82}$$

We make use of the rotational symmetry and represent the variables x,y in the complex plane:

$$z = \tilde{x} - i\tilde{y} = re^{-i\theta}, \qquad \bar{z} = \tilde{x} + i\tilde{y} = re^{i\theta} \tag{83}$$

z and $\bar{z}$ are as independent as x and y, so the Hamiltonian becomes:

$$\mathcal{H} = \frac{1}{2} \left(-4\partial_z\partial_{\bar{z}} + \frac{1}{4}z\bar{z} + \bar{z}\partial_{\bar{z}} - z\partial_z \right) \tag{84}$$

In this way the creation and annihilation operators defined in equation(79) become

$$\hat{a}^\dagger = \frac{1}{\sqrt{2}} \left(-i\partial_{\tilde{x}} - \frac{\tilde{y}}{2} + \partial_{\tilde{y}} + i\frac{\tilde{x}}{2} \right) = \frac{i}{\sqrt{2}} \left(\frac{\bar{z}}{2} - 2\partial_z \right) \tag{85}$$

$$\hat{a} = \frac{1}{\sqrt{2i}} \left(\frac{z}{2} + 2\partial_{\bar{z}} \right)$$

$$\hat{b} = \frac{1}{\sqrt{2}} \left(\frac{\bar{z}}{2} + 2\partial_z \right), \qquad \hat{b}^\dagger = \frac{1}{\sqrt{2}} \left(\frac{z}{2} - 2\partial_{\bar{z}} \right)$$

In the last line we defined another possible linear combination of coordinates and derivatives. This new linear combination does not appear in the Hamiltonian(80).

The additional operators $b, b^\dagger$ will be necessary to express the angular momentum operator in creation and annihilation operators.

$$L_z = (\vec{r} \times \vec{p})_z = -i\hbar(x\partial_y - y\partial_x) \tag{86}$$
$$= \hbar(\bar{z}\partial_{\bar{z}} - z\partial_z) = \hbar(\hat{a}^\dagger\hat{a} - \hat{b}^\dagger\hat{b})$$

$\hat{a}$ and $\hat{b}$ operators commute with each other. For $\hat{a}$ and $\hat{b}$, the following commutation relations are valid

$$[\hat{a}, \hat{a}^\dagger] = 1, \qquad [\hat{b}, \hat{b}^\dagger] = 1 \tag{87}$$

Because of $[H, L] = 0$ the angular momentum and the Hamiltonoperator have the same eigenstates

$$\mathcal{H}|n, m\rangle = \hbar\omega_c \left(n + \frac{1}{2}\right)|n, m\rangle \tag{88}$$

$$L|n, m\rangle = \hbar(n - m)|n, m\rangle \tag{89}$$

$$|n, m\rangle = \frac{(\hat{b}^\dagger)^{n+m}}{\sqrt{(m+n)!}} \frac{(\hat{a}^\dagger)^n}{\sqrt{n!}}|0, 0\rangle \tag{90}$$

The eigenvalue n of $\hat{a}^\dagger\hat{a}$ is called the Landau level. From $\hat{a}|0, 0\rangle = 0$ and $\hat{b}|0, 0\rangle = 0$ the lowest Landau level can be constructed.

$$\hat{a}|0, 0\rangle = \frac{i}{\sqrt{2}}\left(\frac{z}{2} + 2\partial_{\bar{z}}\right)|0, 0\rangle = 0 \tag{91}$$

$$|0, 0\rangle = \frac{1}{2\pi}e^{-\frac{1}{4}z\bar{z}} \tag{92}$$

By raising the m quantum number with $\hat{b}^\dagger$ we can successively create further lowest Landau levels.

$$|0, m\rangle = \frac{(\hat{b}^\dagger)^m}{\sqrt{m!}}|0, 0\rangle = \frac{z^m e^{-\frac{1}{4}z\bar{z}}}{\sqrt{2\pi 2^m m!}} \tag{93}$$

In the same way higher Landau levels $n > 0$ can be produced by applying $\hat{a}^\dagger$. In figure(17) a lowest Landau level in the x-y plane is shown.

Now, since we have calculated the quantum mechanical motion of electrons in a magnetic field we apply an additional homogeneous electric field E in x-direction. In order to obtain some nice demonstrative parallels with the classical electron motion, we transform our coordinates back to $x = \tilde{x}l$.

$$|0, m\rangle = \frac{(x + iy)^m}{\sqrt{2\pi 2^m m! l}}e^{-\frac{1}{4l^2}r^2} \tag{94}$$

Here r^2 is the radial distance in the plane. One can easily see that the ring in figure(17) and in equation(94) has a width of $\Delta r = l$. In the classical case
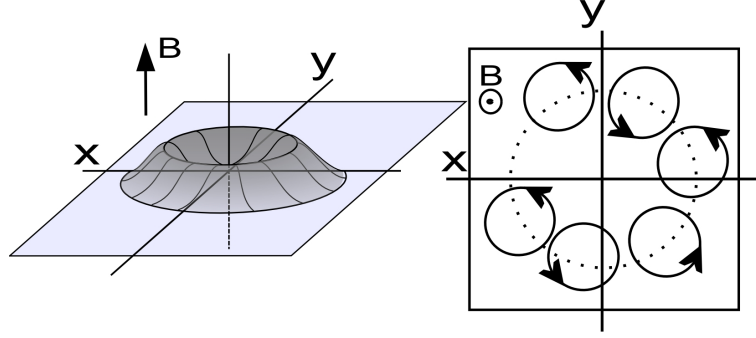
Figure 17: Interpretation of the quantum mechanical Landau state(right) in terms of a classical picture (left). The Landau state is a superposition of cyclotron orbits of radius l with centers around the "ring" of radius $\sqrt{2ml}$ of maximal probability of the Landau level

an electron in a magnetic field moves on a circle with cyclotron frequency $\omega_c = |e|B/mc$

$$\vec{r} = \vec{R}_0 + r_0(\cos(\omega_c t), \sin(\omega_c t), 0) \tag{95}$$
$$\vec{v} = r_0\omega_c(-\sin(\omega_c t), \cos(\omega_c t), 0)$$

The kinetic energy of a moving electron is $E_{kin} = \frac{m}{2}v^2 = \frac{1}{2}m\omega_c^2 r_0^2$. Comparing this with the quantum mechanical energy of the lowest Landau level $E_0 = \frac{1}{2}\hbar\omega_c$ we obtain an estimate for the average radius of a cyclotron orbit of a lowest Landau level: $r_0 = l$.

Hence not the ring in figure(17) itself depicts the cyclotron motion, it is rather a superposition of orbits as shown on the left-hand side of figure(17). The expectation value of

$$\langle 0, m|r^2|0, m \rangle = 2(m+1)l^2 \tag{96}$$

gives the radius of the maximum of the ring: $r_{max} = \sqrt{2ml}$.

At the beginning of this section we discussed the Hall effect. A typical hallbar like that in figure(16) is of course only of a finite size. Equation(96) tells us that the radius of the ring increases as the quantum number m is increased. There is a maximal size of the ring, and therfore a maximal m, due to the finite geometry. Let's assume that the hallbar has a rotational symmetry and a size of $S = \pi R^2$. The largest value for m is $m = \frac{R^2}{2l^2}$, and this is also the degeneracy in our system. Related to a unit area, the degeneracy is $\frac{1}{2\pi l^2}$. That means there is one electron state for each area $2\pi l^2$. The magnetic flux which is penetrating the area of an electron is given by

$$\Phi = 2\pi l^2 B = \frac{hc}{|e|} = \Phi_0 \tag{97}$$

which says that there is one electronstate per flux quantum Φ_0. These considerations are also valid for higher Landau levels [27]. It can happen that an electron

shares more than one single flux quantum, and this goes in the direction of the fractional quantum Hall effect.

Furthermore, there is an important quantity in the theory of the quantum Hall effect called the filling factor ν. It relates the two dimensional density of electrons to the degeneracy per unit area.

$$\nu = \frac{n_e}{1/(2\pi l^2)} = \frac{n_e}{B/\Phi_0} \tag{98}$$

The filling factor is equal to the number of occupied Landau levels at a given magnetic field. When the magnetic field is increased, more and more electrons can be accumulated in one Landau level, hence fewer Landau levels will be occupied. At last, we will apply an electric field in the x-direction in addition to the magnetic field in the z-direction. This corresponds to the situation in a Hall experiment. Now, that the rotational symmetry is broken by the electric field, the symmetric gauge is no longer useful. Instead of the symmetric, we will use the Landau gauge for the vector potential $\vec{A}$.

$$\vec{A}(\vec{r}) = (0, Bx, 0) \tag{99}$$

The Hamiltonian of this problem is

$$\mathcal{H} = \frac{1}{2m}\left(p_x^2 + \left(p_y - \frac{e}{c}Bx\right)^2\right) - eEx \tag{100}$$

The mass m in the denominator in front of the momentum should not be confused with the radial quantum number from above. In the following this quantum number does not appear so there is no source for mistakes. Obviously, we have translational symmetry in the y-direction, so we state the following ansatz:

$$\varphi(\vec{r}) = \frac{1}{\sqrt{W}}e^{ik_y y}\psi(x) \tag{101}$$

W is the length of the system in y direction, i.e. the width of the Hall bar in fig(16). We plug (101) into equation(100) and get the Schrödinger equation for $\psi(x)$.

$$\left(\frac{1}{2m}\left[p_x^2 + (\hbar k_y - \frac{e}{c}Bx)^2\right] - eEx\right)\psi(x) = \epsilon\psi_x \tag{102}$$

Moreover, we introduce the center coordinate X

$$X = -k_y l^2 + \frac{eEml^4}{\hbar^2} \tag{103}$$

This allows us to write the Schrödinger equation in the harmonic oscillator form.

$$\left(\frac{1}{2m}p_x^2 + \frac{m\omega_c^2}{2}(x - X)^2\right)\psi(x) = \left[\epsilon_n + eEX - \frac{m}{2}\left(c\frac{E}{B}\right)^2\right]\psi(x) \tag{104}$$

This time we will give the solution in terms of Hermite polynomials
$H_n(x) = (-1)^n e^{x^2} \frac{d^n}{dx^n} e^{-x^2}$

$$\varphi(\vec{r}) = \frac{1}{\sqrt{W}} e^{ik_y y} \left(\frac{1}{\pi}\right)^{1/4} \left(\frac{1}{2^n n! l}\right)^{1/2} \exp\left(-\frac{(x-X)^2}{2l^2}\right) H_n\left(\frac{x-X}{l}\right) \quad (105)$$

Furthermore, the eigenenergies are given by equation(104):

$$\epsilon_n = \underbrace{\left(n + \frac{1}{2}\right) \hbar\omega_c}_{E_{cyclotron}} - \underbrace{eEX}_{E_{pot}} + \underbrace{\frac{m}{2}\left(c\frac{E}{B}\right)^2}_{E_{kin}} \quad (106)$$

The first part of the eigenenergy(106) $E_{cyclotron}$ is the cyclotron energy, the second one, E_{pot} is the potinetial energy in the electric field and the last one E_{kin} is the kinetic energy of the drift motion in y-direction with velocity $v = c\frac{E}{B}$. Because the crossed fields B, in the z-direction and E, in the x-direction force the electron in the y-direction, just like in the classical case.

From equation(105) we are able to calculate the expectation value of the velocity in x- and y-direction([27]p.29) $< \varphi(\vec{r})|v_x|\varphi(\vec{r}) > = 0$ and $< \varphi(\vec{r})|v_y|\varphi(\vec{r}) > = -E/B$.

Combining these results, $\vec{j} = en_e v$ and ohm's law $\vec{j} = \sigma\vec{E}$, we evaluate the coefficients of the conductivity tensor σ.

$$j_x = en_e v_x = 0 \quad (107)$$
$$j_y = en_e v_y = -en_e cE/B$$
$$\Rightarrow \sigma_{xy} = -\sigma_{yx} = -\frac{j_y}{E_x} = \frac{en_e c}{B}$$

All other coefficients of the two dimensional conductivity tensor are zero. This Hall conductivity, equation (108), does not show any tendency to quantization. If we assume that all Landau levels ϵ_n from $n = 0, ..., n-1$ are completely filled up to the (n-1)th level, then the electron density is $n_e = n/(2\pi l^2)$. The Hall conductivity (108) now becomes

$$\sigma_{xy} = \frac{enc}{2\pi l^2 B} = \frac{e^2}{h} n \qquad n \in \{0, 1, 2, ...\} \quad (108)$$

Although this is exactly the observed value for the Hall conductivity, up to this point we are still far away from understanding the Hall quantization. This is no explanation because important questions remain open, in particular those which will be summerised in the beginning of the next subsection:

• Why are Landau levels always completely filled?

42

- Why is there ballistic transport in x-direction in the plateau regime whereas there is Joule heating and a finite resistance at the transition of two Hall plateaus?

- What kind of role do the always present impurities play?

4.2 The Hall Effect and Electrons in electric and magnetic Fields

To begin with, we consider the experimental setup given in figure(16). To recapitulate the classical Hall effect, imagine a current density $\vec{j} = e n_e \vec{v}$ injected from the right, e is the charge, n_e the charge carrier density and $\vec{v}$ the velocity. There is a potential difference V between 1 and 2 in figure(16) and a perpendicular magnetic field of strength B applied on the sample, due to the Lorentz force

4.3 The Integer Quantum Hall Effect

To start with an explanation of the quantum Hall effect, we first summerize some experimental facts whose explanation will be the aim of this subsection.
In figure(15) the first experimental Hall measurements can be seen. One can clearly see the plateaus of σ_{xy} appearing at integer multiples of the conductance quantum e^2/h. Throughout the Hall plateaus the longitudinal resistivity ρ_{xx} remains zero, whereas at the transition there is a finite Joule heating and therefore a finite resistivity. At this point one should point out that the resistivity is a tensorial quantity.

$$\vec{j} = \sigma \vec{E} \qquad \sigma = \rho^{-1} \tag{109}$$

In this sense, it should be explicitly said that zero resistivity by no means implies a perfect conductance $\sigma = \infty$. This follows from a simple calculation. $\sigma_{xx} = \sigma_{yy}$ and $\sigma_{xy} = -\sigma_{yx}$.

$$\sigma = \begin{pmatrix} \sigma_{xx} & \sigma_{xy} \\ -\sigma_{xy} & \sigma_{xx} \end{pmatrix} \qquad \rho = \sigma^{-1} = \begin{pmatrix} \frac{\sigma_{xx}}{\sigma_{xx}^2 + \sigma_{xy}^2} & -\frac{\sigma_{xy}}{\sigma_{xx}^2 + \sigma_{xy}^2} \\ \frac{\sigma_{xy}}{\sigma_{xx}^2 + \sigma_{xy}^2} & \frac{\sigma_{xx}}{\sigma_{xx}^2 + \sigma_{xy}^2} \end{pmatrix} \tag{110}$$

The longitudinal resistance vanishes if the diagonal conductance σ_{xx} is zero. In the case of our Hall plateaus both the longitudinal resistivity and conductivity are zero. By the way, the conductance and the conductivity have the same physical units in real two dimensional systems.

Two dimensional structures for an observation of the quantum Hall effect are usually given by heterostructures or quantum wells. We will not get deep into the certain realisations because in the case of graphene we already know how two

dimensional structures are produced. So far, all usual systems are semi-conductor sandwich structures where electrons live in a small layer at an interface. The degree of freedom in the z direction is frozen because the excitation gap is too large to become overwhelmed. Just think of an infinite potential well with very tiny extent in the z direction. Furthermore the electrons do not feel the lattice of the semi-conductor which makes them really a free two dimensional electron gas.

So far we considered the fundament of the quantum Hall effect. In particular the motion of a single electron in constant magnetic and electric fields. This suffices already because the quantum Hall effect can be explained in a single particle framework. We do not need to take into account interactions between electrons, although they are present. They might alter quantitatively some features but not qualitatively.

Now the more important question is what kind of role do the edge and impurities in the bulk of the sample play in an explanation of the quantum Hall effect. Because of the fundamental quantities e and h appearing in the quantized conductivity one might tend to say that impurities and edges play the role of corrections. But surprisingly, they lie at the heart of the quantum Hall effect.

4.3.1 The Effect of weak Disorder and magnetic Fields in the Bulk

We consider a Hall bar of a finite size spangled with impurities creating a whole mountain range on the sample. This influence on the Landau level structure is given in equation(111), below:

$$\epsilon_n = \left(n + \frac{1}{2}\right)\hbar\omega_c + V(\vec{R}) \tag{111}$$

Thus, the degeneracy of the Landau levels is lifted. There are eigenstates with energies between the Landau level, blurring up the sharp lines, fig.(18). The mountains and valleys in the sample are visualized on the lower right and left in figure(19).

Without any magnetic field electrons and holes in two dimensions experience Anderson localization. That means although the charge carriers seem to be free on atomic scales, they are localized on a greater scale due to interference effects of the wave function. As the size of the system becomes macroscopic the wave function of a charge carrier does not extent from one end to the other. Hence in two dimensions the conductance should be zero.

What changes in the case where a large magnetic field is switched on?

In the last subsection we introduced the magnetic length $l^2 = \frac{\hbar c}{|e|B}$. The magnetic length l resambles the radius of cyclotron motion of a classical particle in a magnetic field. As the magnetic field increases, l becomes smaller and smaller. Thus, at a certain field strength B, the magnetic length becomes small compared

to the disordered impurity potential. Consequently, this random potential has a smooth behaviour on the scale of l. From a semi-classical point of view, the electron experiences a crossed magnetic field B and electric field $E = \frac{\partial V(\vec{r})}{\partial \vec{r}}$, $V(\vec{r})$ is the random potential. As a result the electron moves on an equipotential line. In view of figure(19), if an electron has an energy which falls into the region of valleys or hills respectively, then the motion is closed and the state belonging to this energy is localized.

Intuitively we can compare the filling of levels denoted by the energy(111) with filling of a landscape with water[15]. This is visualised in figure(19). At first, there is only a formation of small unconnected lakes due to the filling of valleys. These states are localized and do not contribute to the current. After a while the lakes become connected and small rivers carrier water from one end to the other. This is the percolation threshold, at which the states contribute to the current. A further filling just occupies the states on the hill which do not contribute as stated above. This procedure repeats with the next Landau level.

A more sophisticated investigation is given by numerical calculations ([9] p.97) and ([27] p.34). From these calculations the localization length ξ, i.e. the extent of the electronic wave function in such a random potential, as a function of the energy ϵ can be obtained and compared with the size of the sample L. The localization length of the lowest Landau level is given by:

$$\xi(\epsilon) \propto |\epsilon - \epsilon_c|^{-\alpha}, \qquad \alpha = 2.3 \pm 0.1 \tag{112}$$

ϵ_c denotes the energy at the center of a Landau level. As long as $L < \xi(\epsilon)$, the electronic wave function extents over the whole sample and connects both ends. So far we obtained an arrangement of two kinds of states, localized states and a very narrow region of extended states. The energy gap created by the formation of Landau levels vanished, leaving behind a mobility gap, fig.(18). This model explains somewhat the formation of Hall plateaus in an intuitive way but it fails to explain Hall conductivity. Because of the very narrow energy band of localized states, there are only very few electrons n_{extend} contributing to the current. The Hall conductance behaves like $\sigma_{xy} = ecn_{extend}/B$ and the density of extended states n_{extand} is quite far away from the total number of occupied Landau levels per sample size $n/(2\pi l^2)$. This model would only work if we introduce a certain mechanism that tells the hallbar to behave like a disorder free sample in the mobility gap. Hence, the electrons occupying the Landau levels crossed so far contribute to the current. Whereas it puts all additional electrons in localized states, which do not contribute to the current $\sigma = const.$, until the next Landau level is crossed and all the states below that energy begin to behave like disorder free extended one.

The next part treats the effect of edges. It is known as the Landauer-type explanation([9]p.83) or Büttiker's Theory([27]p.41) and will give us a more satisfying

[15]Here we consider the magnetic field B to be constant and we vary the electron density with the back gate voltage
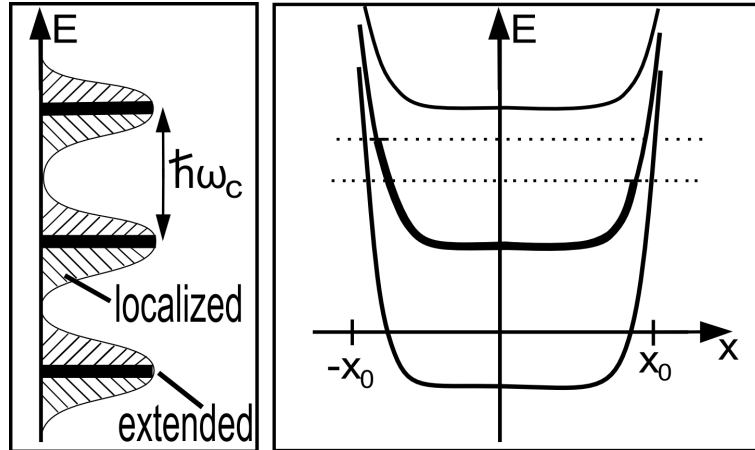
Figure 18: (right) Structure of Landau levels in a system with weak disorder. Extended states at $\hbar\omega_c(n + 1/2)$ and localized states between. (left) Landau levels of a sample with edges. Due to the confining potential of the sample, edge current states can be occupied between the energies of the bulk. The dotted line indicate the different occupation of states of the left and the right edge due to a difference in chemical potential $\Delta\mu$ at the leads

explanation. That does not mean that this part was unnecessary, because parts of this disscussion are also implemented in other explanations.

4.3.2 The Effect of the Edges

The electrons inside the Hall bar are confined in the y-direction because the sample has finite size. Thus the potential raises at the edges, just as indicated in figure(18).
Once more we go back to classical physics to get an idea of what happens at the edges. We have seen that in a magnetic field, an electron denotes a circle when it moves in the bulk. If it comes too near to the edges, the strong ascent of the confining potential acts like an infinitely high wall and the electron bounces off, doing another half circle till it touches the wall again. This can be seen in figure(19) on the top. In this way we get two currents moving in opposite directions at the two edges. Furthermore, this effect suppresses backscattering at the edges giving rise to ballistic transport.

Going back to quantum mechanics, we see in figure(19) schematically that the weak disorder heavily effects the bulk but has no effect on the edges because of the much higher confining potential. The equipotential lines are hardly altered by the random potential and still connect one end of the sample with the other. Namely, edge states are extended states.
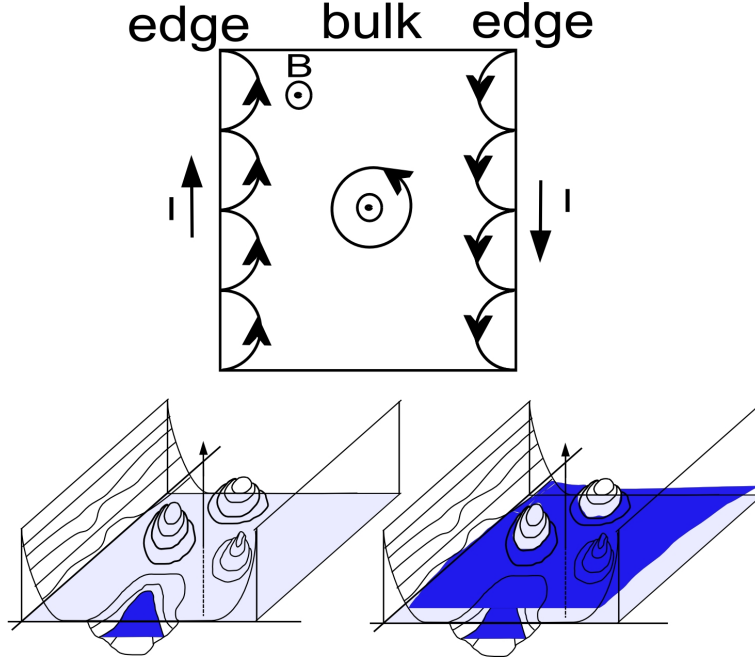
Figure 19: (top) classical motion of edge state and bulk state electrons in a magnetic field. (lower r,l) potential energy landscape of a weakly disordered sample with edges. The z-axis is the energy

However, we are now able to explain the origin of the ballistic transport at the plateaus of σ_{xy} and the finite resistivity at the transitions.

For symplicity we consider here a constant magnetic field, strong enough to observe the quantum Hall effect and vary rather the electron density. In this sense we just raise and lower the Fermi energy bar in figure(18) on the energy axis, and effect the occupation of energy eigenstates. We start in the middle of two Landau levels. The bulk states of (n-1)th Landau level are fully occupied. That means due to the Pauli principle, which excludes fermions to be in the same state, scattering is not possible and the resistivity is zero in this regime. Due to the difference in the chemical potential $\Delta\mu$, i.e. the applied voltage in x-direction, one edge current is favoured and an edge current is flowing in one direction. As we said in the beginning of this subsection, edge currents are a ballistic transport phenomena and feel no backward scattering. We can calculate this current:

The current density is expressed as

$$\vec{j} = e n_e(\vec{r}) \vec{v}(\vec{r}) \tag{113}$$

where $\vec{v}(\vec{r})$ is the velocity and $n_e(\vec{r}) = \sum_k \delta^{(2)}(\vec{r} - \vec{r_k})$ is the density of electrons. The current density is uniform in the x direction due to translational symmetry[16].

---

[16]We consider only the edges where disorder has small effects

The current in the x direction is

$$I_x = \int \vec{j}(\vec{r}) \cdot \frac{\vec{x}}{|x|} dy \tag{114}$$

$$= \frac{1}{L} \int \int \vec{j}_x(y) dy dx$$

$$= -\frac{e}{L} \int d^2 r n_e(\vec{r}) v_x(\vec{r})$$

$$= -\frac{e}{L} \sum_k v_x(\vec{r}_k)$$

In this way we define our current operator as

$$\hat{I}_x = -\frac{e}{L} \sum_k \hat{v}_{kx} \tag{115}$$

Later, we will replace the sum by an integal: $\sum_k \to \int \frac{dp_x}{2\pi\hbar}$
In order to obtain an expression for the current we recall equation(100) where we calculated the motion of an electron in electric and magnetic fields. This time we consider the confining edge potential $U(y)$ which is uniform in the x direction. The magnetic field is introduced by the vector potential in the Landau gauge $\vec{A} = (-By, 0, 0)$.
The Hamiltonian with the confining potential is given by

$$\mathcal{H} = \frac{1}{2m} \left[\left(p_x + \frac{e}{c} By \right)^2 + p_y^2 \right] + U(y) \tag{116}$$

From this Hamiltonian we can immediately extract an expression for the velocity operator:

$$m\hat{v}_x = p_x + \frac{e}{c} By \tag{117}$$

Moreover we replace the summation in eq.(115) by an integral over the momentum in x-direction p_x. This kind of counting states is valid, because the center coordinate of the wavefunction depends on p_x, see eq.(105). Consequantly, the current in x direction is given by

$$I_x = -e \int \frac{dp_x}{2\pi\hbar} \langle \hat{v}_x \rangle \tag{118}$$

$$= -\frac{e}{h} \int dp_x \frac{1}{m} \langle p_x + \frac{e}{c} By \rangle$$

$$= -\frac{e}{h} \int dp_x \langle \frac{\partial \mathcal{H}}{\partial p_x} \rangle$$

Instead of evaluating the expectation value of the derivative of the Hamiltonian with respect to the momentum we take the derivative of the expectation value.

$$I_x = -\frac{e}{h} \frac{\partial E}{\partial p_x} = -\frac{e}{h} \int dE = \frac{e}{h} \Delta\mu \tag{119}$$

48

The difference in the chemical potential $\Delta\mu$ can be expressed by the Hall voltage $\Delta\mu = eV_H = eE_yW$. Then, the current density is:

$$j_x = \frac{e}{h}E_y \qquad (120)$$

$$\sigma_{xy} = \frac{e^2}{h}$$

Finally we obtained the current density and conductivity if we settle our fermi energy above the lowest Landau level but still below the next Landau level.

Now imagine, that we raise the fermi energy bar to the point where half of the states of the next Landau level are occupied. Because there are empty states available without any gap, scattering is possible and we have a finite resistivity and Joule heating. We lift the bar further all states become occupied and scattering is not possible because the gap to the next Landau level is too large to be overcome by thermal excitation. Moreover in figure(18) we can see that now the edge states of this next Landau level also contribute to the current. If we have n-1 Landau levels[17] below the Fermi energy then we have n times the current of equation(121) and n times its conductivity

$$\sigma_{xy} = \frac{e^2}{h}n \qquad (121)$$

This is the observed Hall conductivity, and we have finished a somehow intuitive explanation of the interger qunatum Hall effect. However the quantum Hall effect is, except for graphene, only observable at rather low temperatures. when the temperature becomes compareable with the distance of Landau levels $k_BT \sim \hbar\omega_c$, the QHE will be destroyed.

In the next section we will treat the integer quantum Hall effect in graphene, which behaves similar but has some strange unexpected or so to speak unconventional features.

4.4 The unconventional Quantum Hall Effect in Graphene

In the last section we discussed the behaviour of charge carriers confined on a two dimensional plane under the influence of a crossed electric and magnetic field. The quantum Hall effect appears in the strong magnetic field limit. Since graphene is a real two dimensional electron system, it certainly shows the quantum Hall effect. Therefore the explanation, which was based on semi-conductor devices should hold here, too.

The charge carriers in graphene exhibit a four fold degeneracy. Since the Zeeman splitting is low compared to the energy between two adjacent Landau level[18] all

---

[17]The Landau levels start at zero $0, 1, 2, \ldots$

[18]For $B = 30T$ the Zeeman splitting energy is $2\mu_B B \sim 1meV$, whereas the difference between the lowest Landau level $E_0 = 0$ and the first is $E_1 = \sqrt{2\hbar v_F^2 |e|B} \approx 1eV$.

states are two fold degenerate. Secondly, we have another factor of two emerging from the equal contributions of the K-valleys K^+ and K^-. Consequently, we expect the Hall conductivity quantized in multiples of

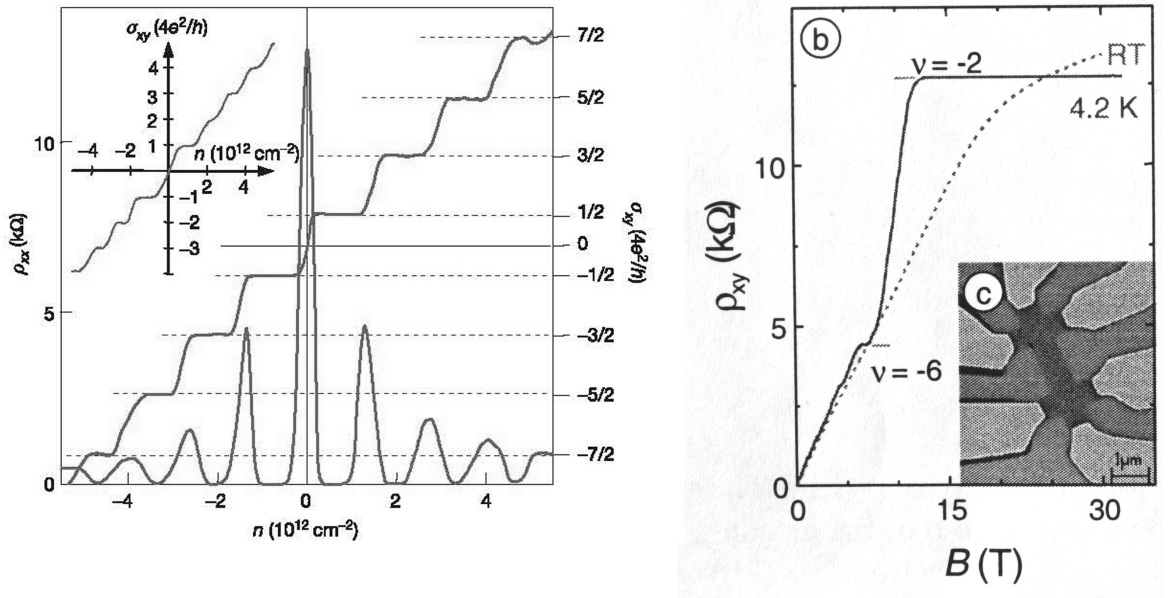$$\sigma_{xy} = 4\frac{e^2}{h} \cdot n \qquad n \in \{\ldots, -1, 0, 1, \ldots\} \tag{122}$$

Figure 20: (left) Measurements of the Hall conductivity σ_{xy} in graphene recorded by K.S. Novoselov, A.K. Geim, et al. [19]. The Hall conductivity and the longitudinal resistivity are plotted against the charge carrier density which can be tuned by the back gate voltage. One can clearly see that the stair like Hall conductivity exhibits plateaus at half-integer multiples of the degenerated conductance quantum $4e^2/h$. The Inset on the upper left shows the same graphs for a bilayer sample, where σ_{xy} increases in integer steps. The right picture was measured by [5]. The Hall conductivity as a function of the magnetic field at $4.2K$ (solid line) and at room temperature(RT) (dotted line). The step at filling factor $\nu = -2$ is present even at room temperature.

Nevertheless, in experiments fig.(20), a Hall conductivity of

$$\sigma_{xy} = 4\frac{e^2}{h}\left(n + \frac{1}{2}\right) = \nu\frac{e^2}{h}, \qquad \nu = 4\left(n + \frac{1}{2}\right) \tag{123}$$

is observed and not eq.(122). Namely, the integer quantum Hall effect (IQHE) appears at half-integers.
Like most of the usual qunatum phenomena, the IQHE appears at very low temperatures. In conventional semi-conductor heterostructures, no QHE has ever

been observed above $T = 30K$ since localisation will be fully destroyed if the temperature is further increased. Unlike those materials the IQHE in graphene appears at room temperature. This is demonstrated in the diagramm on the right hand side of figure(20), where the Hall conductivity has a still visible step at room temperature.

Beside this half-integer QHE regime [10] reported Hall plateaus at filling factors $\nu = 0, \pm 1$ in addition to the $\nu = 4(n + 1/2)$. These new quantum Hall(QH) states are observalble at very high magnetic fields $(B > 20T)$ and appear only in samples of the highest quality with mobilities larger than $15000cm^2/Vs$.

All these observations which deviate from the QHE in semi-conductors have origininate from the ultra relativistic massless charge carriers. In order to explain the phenomena listed above, we will derivate an expression for the energy of Landau levels.

In section(3) we obtained an expression for the Langrangian, equation(51), of the low energy quasi particles. In the following we will omit the spin dependance, keeping in mind the spin degeneracy in the Hall conductivity. Hence the Zeeman term in eq.(51) will be neglected. Furthermore, from the Langrangian(51) we derivate the equation of motion for the field operators. In the following we will work in the first quantized picture and deal with wavefunctions and not with field operators. However, this procedure gives us two equation for the wavefunction at K^+ and K^- points.

$$\left[i\tau^0\hbar\partial_t + i\hbar v_F\tau^1 D_1 + i\hbar v_F\tau^2 D_2\right]\Psi_{K+}(t, \vec{r}) = 0 \tag{124}$$

$$\left[i\tau^0\hbar\partial_t - i\hbar v_F\tau^1 D_1 - i\hbar v_F\tau^2 D_2\right]\Psi_{K-}(t, \vec{r}) = 0 \tag{125}$$

Here, we used the covariant derivative $D_\alpha = \partial_\alpha + \frac{ie}{\hbar c}A_\alpha$. Next, we multiply the first equation(124) by τ_3 and the second equation(125) by $-\tau_3$ and get almost the same equation for both K-points:

$$\left[\pm i\hat{\gamma}^0\hbar\partial_t + i\hbar v_F\hat{\gamma}^1 D_1 + i\hbar v_F\hat{\gamma}^2 D_2\right]\Psi_{K\pm}(t, \vec{r}) \tag{126}$$

The $\hat{\gamma}$ matrices in (126) are:

$$\hat{\gamma}^0 = \begin{pmatrix} 1 & 0 \\ 0 & -1 \end{pmatrix} \qquad \hat{\gamma}^1 = \begin{pmatrix} 0 & 1 \\ -1 & 0 \end{pmatrix} \qquad \hat{\gamma}^0 = \begin{pmatrix} 0 & -i \\ -i & 0 \end{pmatrix} \tag{127}$$

Now we will solve the equation for the K^+ point, the solution of K^- will differ by a sign. We split the 2-spinor into its sublattice parts:

$$\Psi_{K+} = \begin{pmatrix} \varphi \\ \psi \end{pmatrix} \tag{128}$$

We plug this 2-spinor into equation(126) and obtain the following system of equations:

$$\begin{pmatrix} \dot{\varphi} \\ \dot{\psi} \end{pmatrix} = \begin{pmatrix} 0 & W \\ Z & 0 \end{pmatrix} \begin{pmatrix} \varphi \\ \psi \end{pmatrix} \tag{129}$$

with

$$W = -v_F \left(\partial_x + \frac{ie}{\hbar c} A_x \right) + i v_F \left(\partial_y + \frac{ie}{\hbar c} A_y \right) \tag{130}$$

$$Z = v_F \left(\partial_x + \frac{ie}{\hbar c} A_x \right) + i v_F \left(\partial_y + \frac{ie}{\hbar c} A_y \right)$$

Instead of first order differential equations we solve a second order differential equation for φ and ψ:

$$\ddot{\varphi} = W Z \phi \tag{131}$$
$$\ddot{\psi} = Z W \psi$$

We make an ansatz for the time dependance of psi:

$$\psi(t, \vec{r}) = e^{-iEt/\hbar} \psi(\vec{r}) \tag{132}$$

If we plug this ansatz into the differential equation for ψ eq.(132) and use the symmetric gauge for the vector potential $\vec{A} = B/2(-y, x, 0)$:

$$\ddot{\psi} = -\frac{E^2}{\hbar^2} \psi(\vec{r}) = v_F^2 \left[-\left(\partial_x + \frac{i}{l^2} \frac{y}{2} \right)^2 - \left(\partial_y - \frac{i}{l^2} \frac{x}{2} \right)^2 - \frac{1}{l^2} \right] \psi(\vec{r}) \tag{133}$$

In equation(133) we introduced the magnetic length $l^2 = \hbar c/(|e|B)$. We multiply equation(133) by $\hbar^2$, introduce dimensionless coordinates $x \to x/l$ and play a little bit with the righthand side:

$$\hbar^2 \frac{v_F^2}{l^2} \left[\left(-i\partial_x - \frac{y}{2} \right)^2 + \left(-i\partial_y + \frac{x}{2} \right)^2 - 1 \right] \tag{134}$$
$$= \hbar^2 \frac{v_F^2}{l^2} \left[\left(-4\partial_z \partial_{\bar{z}} + \frac{1}{4} z\bar{z} - z\partial_z + \bar{z}\partial_{\bar{z}} \right) - 1 \right]$$
$$= \hbar^2 \frac{v_F^2}{l^2} \left[2 \cdot \left(\hat{n} + \frac{1}{2} \right) - 1 \right]$$
$$= \hbar^2 \frac{v_F^2}{l^2} [2n]$$

In the second line of equation(135) we introduced a complex notation $z = y - ix$, similar to the last section. In the same sense we introduced creation and annihilation operators and the occupation number operator $\hat{n}$. All in all, we gain an expression for the energy of the Landau levels of relativistic massless particles.

$$E_n = sgn(n) \sqrt{v_F^2 \hbar |e| B 2n/c} \tag{135}$$

Moreover, we can easily obtain the energy for φ: $E_n = sgn(n)\sqrt{v_F^2\hbar|e|B2(n+1)/c}$. At the K^- points these relations are inverted because the different definition of the 2-spinor Ψ_{K^-} where the sublattice entries are swapped (eq.(42)). Suppose n is positiv, then we are in the electron regime and E_n is positiv. Now we can use the energy of Landau levels for an explanation of the half-integer QHE. The lowest Landau level E_0 is zero for equation(135) but for φ, $E_0 = \sqrt{v_F^2\hbar|e|B2/c}$ is nonzero. Hence the lowest Landau level exhibits half the degeneracy of the other levels and gives only half of the contribution of the other Landau levels. One can also say that the lowest Landau level is equally shared by electrons and holes. Calculations of the Hall conductivity, using the linear response theory and the Kubo formular [6] also show that the unusual Hall conductivity pattern is caused by the lowest landau level which exhibits half the degeneracy of the higher Landau levels.

The high-temperature QHE can be explained by the large energy gap between the lowest and the first Landau level:

$$\sqrt{2\hbar v_F^2 eB} \approx 0.2eV \tag{136}$$

The electrons in a typical $GaAs$ sample have an effective mass of $m^* = 0.067m_e$. The difference between two Landau level is constant: $\hbar\omega_c \approx 1meV$. The QHE is destroyed when the tempeature becomes compareable to this value. At room temperature we have an energy of about $20meV$ which explains the vanishing QHE in semiconductors.

The zero energy Landau level $E_0 = 0$ can also be examined by the Atiyah-Singer index theorem [23]. This theorem is used in quantum field theory to relate functional integrals with the difference between right- and left-handed zero modes of an operator, namely the index of that operator. In this way calculations depend only on topological properties and can often be simplified. In our case the gauge field is the vector potential $\vec{A}(\vec{r})$ and the operator is the Dirac operator $\mathcal{D}$ from section(3) (for example eq.(48)). D is an elliptic operator over a two dimensional manifold $\mathcal{M}$, where $\mathcal{M}$ is the graphene sheet. For even dimensional manifolds, the spinor space is reducible and can be splitted in two irreducible ones. Namely, the two $K^\pm$ contributions in equation(42). The kernel $kern(\mathcal{D})$ of an operator is the set of states with zero energy. The index $ind(\mathcal{D}$ is the difference between the number of zero states at K^- and K^+ valleys. The Atiyah-Singer index theorem says:

$$ind(\mathcal{D}) = dim(kern(\mathcal{D}\mid_{K^+})) - dim(kern(\mathcal{D}\mid_{K^-})) = \frac{1}{2\pi}\int\int B(x,y)dxdy \tag{137}$$

$B(x,y)$ is the magnetic field, pointing in the z-direction. We can easily carry out the integration on the right hand side ($\Phi = \frac{hc}{e}$ is the flux quantum):

$$\int\int dxdyB(x,y) = \frac{hc}{e}(N+\epsilon) \qquad 0 < \epsilon < 1 \tag{138}$$

In [1] there two nice theorems derivated from (137) and (138).

- If $N + \epsilon > 1$, then there are exactly N-1 zero-energy states whose spin has the same sign as the flux.

- All nonzero energy eigenstates are degenerate with respect to spin flip

Consequently, the zero-energy states in graphene are protected by topological arguments. The narrow $E_0 = 0$ Landau level, staying sharp even at high temperatures, which was observed in [5] can be seen as a direct manifestation of the Atiyah-Singer index theorem. Moreover, these results are important in the case of corrugated graphene layers because it guarantees the robustness of the zero-energy Landau states. The analysis of weak localization measurements [18] have shown that the ripples cause a random gauge field and that graphene should behave as if it were exposed to a random magnetic field from approximately $0.1T$ to $1T$.

Further analysis of the integer quantum Hall effect with more sophisticated methods like the nonlinear sigma model, as done by [22], relate the non-standard quantization to some special symmetry that is preserved by the disorder. For example, they found out that a smooth random potential does not lead to coupled K-valleys, thus suppressing inter-valley scattering. Mechanisms, like electron scattering due to charged impurities lead to inter valley scattering and to the ordinary QHE. However, the theory of the IQHE in graphene is said to be not established yet [22].

Finally, this shows that results from section(2) and (3), ripples and chirality become important in an explanation of the quantum Hall effect.

5 Conclusion

To conclude, we have seen why graphene was found so late, although the cleavage technic at first may seem rather simple. The discussion about the stability of graphene pointed out that the material is corrugated, and that even the stability of graphene can be a tricky question. Furthermore, the low energy expansion of the dispersion relation has shown that the quasi-particles form a real two dimensional gas of massless, ultra-relativistic particles with the same structure as massless neutrinos. Finally, the analysis of the unconventional quantum Hall effect in graphene combined parts from all previous sections showing that effective ultra-relativistic systems exhibit a clearly distinct behaviour compared to the well known two dimensional electron gas in semi-conductors. Although most of these problems are still not completely solved, studying graphene is certainly rewarding.

References

[1] Y. Aharonov and A. Casher. Ground state of a spin-1/2 charged particle in a two-dimensional magnetic field. *Phys. Rev. A*, 19(6):2461–2462, Jun 1979.

[2] Ben Simons Alexander Altland. *Condensed Matter Field Theory*. Cambridge University Press, 2006.

[3] A. Fasolino, J.H. Los, and M.I. Katsnelson. Intrinsic ripples in graphene. *arXiv:0704.1793v1*, 2007.

[4] A.K. Geim and K.S. Novoselov. The rise of graphene. *naturematerials*, 6:183–191, March 2007.

[5] A. J. M. Giesbers, U. Zeitler, M. I. Katsnelson, L. A. Ponomarenko, T. M. Mohiuddin, and J. C. Maan. Quantum-hall activation gaps in graphene. *Physical Review Letters*, 99(20):206803, 2007.

[6] V. P. Gusynin and S. G. Sharapov. Unconventional integer quantum hall effect in graphene. *Physical Review Letters*, 95(14):146801, 2005.

[7] Suzuura, Hidekatsu and Ando, Tsuneya. Crossover from Symplectic to Orthogonal Class in a Two-Dimensional Honeycomb Lattice. *Phys. Rev. Lett.*, 89(26):266603, Dec 2002.

[8] V.P. Gusynin, S.G. Sharapov, and J.P. Carbotte. Ac conductivity of graphene: From tight-binding model to 2+1 dimensional quantum electrodynamics. *arXiv:0706.3016v2(cond-mat.mes-hall)*, Nov 2007.

[9] Jainendra K. Jain. *Composite Fermions*. Cambridge University Press, 2007.

[10] Z. Jiang, Y.-W. Tan, H.L. Stormer, and P. Kim. Quantum hall effect in graphene. *solid State Communication*, 143:14–19, July 2007.

[11] Mikhail I. Katsnelson. Graphene: carbon in two dimensions. *materialstoday*, 10(1-2):20–27, Jan-Feb 2007.

[12] K. v. Klitzing, G. Dorda, and M. Pepper. New method for high-accuracy determination of the fine-structure constant based on quantized hall resistance. *Phys. Rev. Lett.*, 45(6):494–497, Aug 1980.

[13] J.M. Kosterlitz and D.J. Thouless. Ordering, metastability and phase transitions in two-dimensional systems. *Phys. Rev. Lett.*, 6:1181–1203, 1973.

[14] Pierre Le Doussal and Leo Radzihovsky. Self-consistent theory of polymerized membranes. *Phys. Rev. Lett.*, 69(8):1209–1212, Aug 1992.

[15] N. D. Mermin. Crystalline order in two dimensions. *Phys. Rev.*, 176(1):250–254, Dec 1968.

[16] N. D. Mermin and H. Wagner. Absence of ferromagnetism or antiferromagnetism in one- or two-dimensional isotropic heisenberg models. *Phys. Rev. Lett.*, 17(22):1133–1136, Nov 1966.

[17] Geim A. K. Katsnelson M. I. Novoselov K. S. Booth T. J. Roth S. Meyer, Jannik C. The structure of suspended graphene sheets. *Nature*, 446:60–63, March 2007.

[18] S. V. Morozov, K. S. Novoselov, M. I. Katsnelson, F. Schedin, L. A. Ponomarenko, D. Jiang, and A. K. Geim. Strong suppression of weak localization in graphene. *Physical Review Letters*, 97(1):016801, 2006.

[19] Geim A. K. Morozov S. V. Jiang D. Katsnelson M. I. Grigorieva I. V. Dubonos S. V. Firsov A. A. Novoselov, K. S. Two-dimensional gas of massless dirac fermions in graphene. *Nature*, 438:197–200, November 2005.

[20] Fernandez, Julio F. Crystalline Stability and Order in One and Two Dimensions *Phys. Rev. B*, 1(4):1345–1350, Feb 1970.

[21] K. S. Novoselov, D. Jiang, F. Schedin, T. J. Booth, V. V. Khotkevich, S. V. Morozov, and A. K. Geim. Two-dimensional atomic crystals. *Proceedings of the National Academy of Sciences*, 102(30):10451–10453, 2005.

[22] P.M. Ostrovsky, I.V. Gornyi, and A.D. Mirlin. Theory of anomalous quantum hall effects in graphene. *arXiv:0712.0597v1 [cond-mat.mes-hall]*, DEC 2007.

[23] Jiannis K. Pachos and Michael Stone. an index theorem for graphene. *arXiv:cond-mat/0607394v4*, Sep 2007.

[24] Franz Schwabel. *Quantenmechanik fuer Fortgeschrittene*. Springer, 2005.

[25] Franz Schwabel. *Quantenmechanik fuer Fortgeschrittene*. Springer, 2005.

[26] Gordon W. Semenoff. Condensed-matter simulation of a three-dimensional anomaly. *Phys. Rev. Lett.*, 53(26):2449–2452, Dec 1984.

[27] D. Yoshioka. *The Quantum Hall Effect.* Springer, 2002.